DENDRITE FORMATION IN RECHARGEABLE LITHIUM-METAL BATTERIES: PHASE-FIELD MODELING USING OPEN-SOURCE FINITE ELEMENT LIBRARY

MARCOS E. ARGUELLO[□,‡,⋆], NICOLÁS A. LABANDA[◇,♠], VICTOR M. CALO[◇], MONICA GUMULYA[▼], RANJEET UTIKAR[□], AND JOS DERKSEN[‡]

ABSTRACT. We describe a phase-field model for the electrodeposition process that forms dendrites within metal-anode batteries. We derive the free energy functional model, arriving at a system of partial differential equations that describe the evolution of a phase field, the lithium-ion concentration, and an electric potential. We formulate, discretize, and solve the set of partial differential equations describing the coupled electrochemical interactions during a battery charge cycle using an open-source finite element library. The open-source library allows us to use parallel solvers and time-marching adaptivity. We describe two- and three-dimensional simulations; these simulations agree with experimentally-observed dendrite growth rates and morphologies reported in the literature.

Keywords: Phase-field modeling, Electrodeposition, Lithium dendrite, Metal-anode battery, Finite element method

CONTENTS

[□] WA School of Mines, Mineral, Energy and Chemical Engineering, Curtin University, P.O. BOX U1987, Perth, WA 6845, Australia.

[‡] School of Engineering, University of Aberdeen, Elphinstone Road, AB24 3UE Aberdeen, United Kingdom.

[◇] School of Electrical Engineering, Computing and Mathematical Sciences, Curtin University, P.O. Box U1987, Perth, WA 6845, Australia

[♠] SRK Consulting, West Perth, Western Australia, Australia.

[▼] Occupation, Environment and Safety, School of Population Health, Curtin University, P.O. Box U1987, Perth, WA 6845, Australia

(⋆) Corresponding author: Marcos E. Arguello, m.arguello@postgrad.curtin.edu.au

E-mail addresses: m.arguello@postgrad.curtin.edu.au, m.arguello.19@abdn.ac.uk , nlabanda@srk.com.au, victor.calo@curtin.edu.au, m.gumulya@curtin.edu.au, r.utikar@curtin.edu.au, jderksen@abdn.ac.uk.

Date: May 10, 2022.

1. Introduction

Conventional lithium-ion batteries (LIB) that use intercalated graphite electrodes have dominated the rechargeable battery market over the past three decades; nevertheless, this battery technology is reaching its theoretical limit of 250 Wh/kg [1, 2]. Therefore, our society has a strong need for new chemistries and designs to achieve commercial implementation of ultra-high energy density batteries of around 500 Wh/kg [3].

Currently, metallic lithium (Li) is the most prominent negative electrode material due to its combined high theoretical energy density (3860 mAh/g) and low reduction potential (-3.04 V vs. standard hydrogen electrode). However, despite recent successful operation reports for lithium metal batteries (LMBs), all reported short life cycles due to uneven and unstable lithium deposition leading to dendrite formation [4, 5]. Therefore, developing a stable rechargeable lithium metal anode is crucial to attaining higher energy density rechargeable technologies, such as Li-air, Li-S, and Li-flow batteries [6, 7].

Lithium dendrites form during the battery charge cycle and can disconnect from the anode, generating "dead lithium" compounds that stop participating in the electrochemical reaction, resulting in loss of Coulombic efficiency [8]. Ultimately, the uncontrolled growth of these lithium dendrites can cause the battery to short-circuit when they become large enough to contact the cathode electrode after penetrating through the separator [9–11]. These critical shortcomings of dendrite formation during electrodeposition processes triggered efforts to control the dendritic pattern formation and improve the electrochemical performance of metal-anode batteries. Different strategies exist, including modifications in the electrode structure, porosity, and defect engineering [12–17], pulsed charge-discharge cycle [18–20], electrode surface morphology modification (roughness and wavenumber) [21], solvent and electrolyte composition [22–28], ionic mass transport and electrolyte management [29–35], controls of internal temperature and pressure [36–38], and stable interfacial coatings [39–41].

The formation of dendrites in Li anodes has been noted to vary considerably from one system to the other. Bai et al. [42] noted the formation of mossy/whiskers-like morphologies at current densities lower than the intrinsic diffusion-limited current density (reaction limited regime, where lithium grows from the base). On the other hand, at higher current densities (greater than the diffusion-limited current density, i.e. transport or diffusion limited regime, where lithium grows from the tip), fractal dendritic morphology or finger-like structures are obtained. Transition from base-controlled mossy structure to tip-controlled dendrite growth was also observed experimentally when under limiting current condition. Further, various 2D numerical simulations have found the formation of spike-like or tree-like structures where dendrite growth was found to occur on multiple branches and in multiple directions. These types of formation, however, have not been observed widely experimentally due to instabilities at the branch structures and mass transfer rate limitations at these regions [43].

The experimental investigation of the lithium dendrite formation in rechargeable metal batteries is challenging [44]. Thus, the combined insights from experiment and simulation enhance our understanding of the mechanisms of dendrite formation and growth in lithium anodes [43, 45, 46]. Within these computational models, the thermodynamic ones include several surface nucleation models based on density functional theory (DFT) that explore the mechanisms of lithium electrodeposition and dendrite suppression. Considering lithium dendrite growth as an inherent property of the metal, these models invoke surface energies and diffusion barriers as keys parameters in determining the specific metal structures growing on electrodes [47–49]. Dynamic models describe the electrochemical propagation of dendrites; for example, the space-charge (migration-limited) models violate the electroneutrality at the dendrite tips leading to high overpotentials and the subsequent formation of ramified electrodeposits [50]. Furthermore, stress and inelastic deformation models simulate the dendrite's surface-tension mitigated growth [51, 52]. Additionally, film growth models apply classical film-growth theory within the lithium anode battery [53, 54], and diffusion-limited aggregation models (DLA) develop fractal shapes using random-walk statistics [20]. The latter successfully modeled extremely low currents without considering surface energy.

Moreover, several phase-field (diffuse-interface) models simulate the morphologic evolution of lithium electrodeposits as a result of reaction-driven phase transformation within the metal anode batteries and describe the dendrite morphologies observed experimentally for low, high and pulsating applied current densities [55–76]. The phase-field method describes and predicts the mesoscale microstructural evolution by implicitly tracking the boundaries and interfaces using an auxiliary function (i.e., the order parameter). These models rigorously incorporate interfacial energy, interface kinetics, and curvature-driven phase

boundary movement. The evolution of the phase-field variables satisfies local equilibrium [77] and free energy minimization [78], leading to nonlinear partial differential equations (PDE's). Different phase-field models of the electrochemical dendrite deposition describe the phase-field evolution using the Cahn-Hilliard equation [79, 80], the Allen-Cahn equation [81], or a modified non-linear Allen-Cahn reaction equation [60]. In [82], the authors present a comprehensive review of the existing phase-field simulations in rechargeable batteries.

Despite continuous efforts, there are several open issues related to the evolution of dendritic patterns in lithium metal electrodes. Most published models solve two-dimensional problems to rationalize the dendritic patterns and suppress their growth [65–68, 70, 74, 77]. Nevertheless, the lithium dendrite morphologies are inherently three dimensional [69, 83, 84]. Thus, simulation tools to study and understand the three-dimensional effects triggering pattern formation are essential. Its application includes enhancing our understanding of the differences between 2D and 3D simulations on the free space effect on the Li-ion diffusion to the anode surface, the surface anisotropy, the electric field distribution, the nuclei distribution, the interaction between neighboring dendrites; and assessing control strategies to prevent the dendrite formation (e.g., 3D porous current collectors hosts) [85–88].

Nevertheless, few attempts to simulate three-dimensional lithium dendrite growth exist in the literature. For instance, [89] develops a 3D growth model for the electrode–electrolyte interface in lithium batteries in the presence of an elastic prestress; the model assesses the linearized stability of planar interface growth. Later, Jang et al. performed stochastic modeling of the three-dimensional effect of applied voltage and diffusion constant on the growth of lithium dendrites [90]. Recently, Yangyang et al. [70] presented a phase-field model to study the three-dimensional effect of the exchange current density on the electrodeposition behavior of lithium metal; however, without focusing on dendritic morphologies. The scarcity of three-dimensional phase-field results is evidence of the complexity and large computational cost involved in solving the highly non-linear set of equations describing coupled electrochemical interactions during a battery charge cycle.

In this paper, we present a 3D phase-field framework to describe the dendritic electrodeposition of lithium. This work constitutes a step toward the physics-based, quantitative models to rationalize hazardous three-dimensional dendritic patterns needed to achieve the commercial realization of Li-metal batteries. Herein, we use several computational efficiency improvements to deliver the 3D simulations at a reasonable cost, such as time step adaptivity strategy, mesh rationalization, parallel computation, and balanced phase-field interface thickness to mesh resolution ratio.

We organize the paper as follows: Section 2 presents the basic equations describing the lithium-battery dendrite growth process. Then, we derive the weak variational statement and its numerical implementation in Section 3. We describe the time-adaptive strategy and the parameters that deliver convergence in Section 4 and detail its implementation in Section 5. We discuss numerical simulations of lithium-battery dendrites growth in Section 6, where we validate a two-dimensional model in terms of dendrite propagation rates and spatial distribution analysis of the system's variables in comparison with phase-field simulation results reported in the literature. Furthermore, we simulate three-dimensional spike-like lithium structures that grow under high current density [69, 83, 84] (fast battery charge); these structure's growth is dangerous for battery operation. We perform single and multiple nuclei numerical experiments to study the 3D distribution of the electric field and the lithium-ion concentration to understand the mechanism behind tip-growing lithium morphologies better. Finally, we draw conclusions in Section 7.

2. Governing partial differential equations

We model a battery cell composed of a solid pure Lithium metal anode and a binary liquid electrolyte. The variables of interest are the lithium concentration, ζ, and the electric potential, ϕ. Under an electro potential difference $\Delta\phi$, the battery charges and the electrolyte dissociates in Li^+ cation and A^- anion species; Faradic reactions occur, the current passes through the electrode-electrolyte interface, the Li^+ cation gains an electron and deposits on the anode surface ($Li^+ + e^- \rightarrow Li$). Thus, the physical processes involved in the electrochemical deposition of Lithium are charge and mass transport. The Butler-Volmer kinetics (1) is a standard phenomenological model that describes the charge and mass transport at the electrode-electrolyte interface [91, 92], known as the current-overpotential equation:

$$i = i_0 \left(e^{-\frac{\alpha n F \eta}{RT}} - e^{\frac{(1-\alpha)n F \eta}{RT}} \right) ,$$

(1)

where i is the current density and i_0 is the exchange current density, identified as an intrinsic kinetic parameter and assumed constant in this case [70]. The applied overpotential $\eta(\zeta, \phi)$ is the total free energy change per charge transferred [60]. The first and second term in brackets represent the oxidation and reduction reactions, respectively, whereas α is the charge transfer coefficient that characterizes the forward and reverse reactions [93]. R, T, n, and F represent the gas constant, temperature, valence, and Faraday's constant, respectively. The lithium electrodeposition rate depends on the applied current density via a Faradic reaction [94],

$$(2) \qquad v = \frac{\partial \lambda}{\partial t} = \frac{i}{Fn\mathrm{C}_m^s} \ ,$$

where λ represents the electrodeposited film thickness over a time t, and C_m^s is the site density of Lithium metal (inverse of molar volume) (e.g., see [60, 95] for further details).

2.1. **Phase-field.** We introduce a continuous phase-field variable ξ that corresponds to a dimensionless lithium atom concentration $\widetilde{\zeta} = \zeta/\mathrm{C}_m^s$, with ζ normalized against C_m^s. Thus, $\xi = 1$ and 0 represent the pure electrode and electrolyte phases. Superscripts "s" and "l" represent the solid-electrode and liquid-electrolyte phases. We assume the electrode phase is a pure solid and, thus, neglect the presence of a solid-electrolyte interface (SEI). Consequently, neither species nor charge can be stored at the electrode-electrolyte interface. Therefore, ξ is a non-conserved order parameter in our model [61], satisfying the Allen-Cahn reaction (ACR) model: $\frac{\partial \xi}{\partial t} = \mathcal{R}\left(\frac{\delta \Psi}{\delta \zeta_i}\right)$, where Ψ is the total free functional, expressed as the summation of the Helmholtz free energy density f_{ch}, surface energy density $\mathrm{f}_{\mathrm{grad}}$, and electrostatic energy density $\mathrm{f}_{\mathrm{elec}}$ [56, 60, 79, 80]

$$(3) \qquad \Psi = \int_V \left[\mathrm{f}_{\mathrm{ch}}\left(\xi, \zeta_i\right) + \frac{1}{2}\kappa\left(\xi\right)\left(\nabla \xi\right)^2 + \mathrm{f}_{\mathrm{elec}}\left(\xi, \zeta_i, \phi\right) \right] dV \ ,$$

where ζ_i represents the set of concentrations of all the ionic species, e.g., lithium cation ζ_+, and anion ζ_-, respectively. $\mathrm{f}_{\mathrm{elec}} = \rho\phi$ is the electrostatic energy density, where $\rho = \sum_i n_i F \zeta_i$ is the charge density. The Helmholtz free energy density relative to the standard state is [60, 67],

$$(4) \qquad \mathrm{f}_{\mathrm{ch}} = W\xi^2\left(1 - \xi\right)^2 + C_0 RT \left(\widetilde{\zeta}_+ \ln \widetilde{\zeta}_+ + \widetilde{\zeta}_- \ln \widetilde{\zeta}_- \right) \ ,$$

with ion concentrations, $\widetilde{\zeta}_+ = \zeta_+/C_0$ and $\widetilde{\zeta}_- = \zeta_-/C_0$, being normalised against the initial bulk concentration of Lithium in the electrolyte C_0. We model the equilibrium states using a double-well function $g(\xi) = W\xi^2\left(1 - \xi\right)^2$, where $W/16$ acts as a barrier between the states [64].

The surface energy anisotropy plays an important role in the morphology of the electrodeposit [65], which we implement using a standard approach [63, 96] with $\kappa(\xi) = \kappa_0 \left[1 + \delta_{\mathrm{aniso}} \cos\left(\omega\theta\right)\right]$, where κ_0 relates to the Lithium surface tension γ; δ_{aniso} and ω, are the strength and mode of anisotropy, respectively [97, 98]. θ is the angle between the surface normal and the crystallographic orientation of the lithium dendrite; aligned with the "x" direction of the cell stack for simplicity, as Figure 1 shows. We use four-fold anisotropy ($\omega = 4$) in agreement with lithium body centred cubic crystal structure [65]. We make use of trigonometric identities to arrive to $\cos\left(4\theta\right) = 8n_1^4 - 8n_1^2 + 1$, where $n_1 = \nabla_x \xi / ||\nabla \xi||$. Therefore, the 2D gradient coefficient is,

$$(5) \qquad \kappa(\xi) = \kappa_0 \left[1 + \delta_{\mathrm{aniso}}\left(8n_1^4 - 8n_1^2 + 1\right)\right] \ .$$

Figure 1 sketches (5), showing its preferred growth directions of a lithium electrodeposit ($\theta = 0°, 90°, 270°$) due to four-fold surface energy anisotropy, tending to grow fractal or branched dendrites. In 3D, we use version of (5) (four-fold anisotropy) derived by William et al. [99, 100] to simulate crystal growth

$$(6) \qquad \kappa(\xi) = \kappa_0\left(1 - 3\delta_{\mathrm{aniso}}\right)\left[1 + \frac{4\delta_{\mathrm{aniso}}}{1 - 3\delta_{\mathrm{aniso}}}\left(n_1^4 + n_2^4 + n_3^4\right)\right],$$

where $n_2 = \frac{\nabla_y \xi}{||\nabla \xi||}$ and $n_3 = \frac{\nabla_z \xi}{||\nabla \xi||}$, with "$y$" and "$z$" defined orthogonal to "x" as depicted in Figure 2a

Following [64], we calculate the variational derivative of the free energy functional (3). Thus, the phase-field Butler-Volmer equation matches the velocity of the sharp interface limit of the phase-field equation, with the current-overpotential (1) as follows [59, 65, 101]

$$(7) \qquad \frac{\partial \xi}{\partial t} = -L_\sigma \left[\frac{\partial g(\xi)}{\partial \xi} - \kappa(\xi)\nabla^2 \xi \right] - L_\eta \frac{\partial h(\xi)}{\partial \xi} \left[e^{\left(\frac{(1-\alpha)nF\phi}{RT}\right)} - \widetilde{\zeta}_+ \, e^{\left(\frac{-\alpha nF\phi}{RT}\right)} \right] \ ,$$
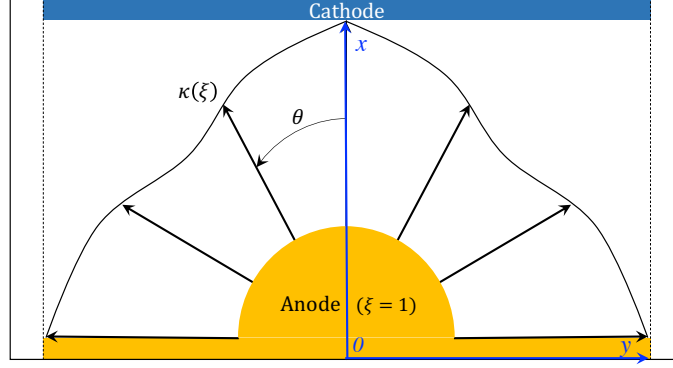
FIGURE 1. 2D schematic of Lithium electrodeposit, with four-fold surface energy anisotropy $\kappa(\xi)$ as a function of θ, defined as the angle between the surface normal and the crystallographic orientation "x".

where we adjust the interface mobility L_σ value (constant for each simulation) for the selected voltage charging the battery. These mobility values balance the phase-field interface energy and the electrochemical reaction contribution [95]. The electrochemical reaction kinetic coefficient is [66]

$$L_\eta = \frac{\gamma i_0}{nF\kappa C_m^s},$$

where the quantities of Li surface energy γ and the phase-field interfacial thickness δ_{PF} relate to the model parameters according to $\delta_{PF} = \frac{2\kappa_0}{3\gamma}$ [102]. The interpolation function $h(\xi)$ smooths the diffuse interface in the current implementation; we use a sigmoid interpolation function [95, 103], which has better computational efficiency than the popular choice of polynomial interpolation function [104]:

$$(8) \qquad h(\xi) = \frac{e^{\varsigma\left(\xi-\frac{1}{2}\right)}}{1 + e^{\varsigma\left(\xi-\frac{1}{2}\right)}},$$

where ς is a parameter that determines the interface thickness of the interpolation function; we use $\varsigma = 20$, to adjust for interpolation between $\xi = 0$ and $\xi = 1$.

2.2. **Diffusion-migration process.** A diffusion-migration equation describes the motion of charged chemical species (lithium-ion) in the fluid electrolyte. The temporal evolution of $\widetilde{\zeta}_+$, satisfies the modified Nernst-Planck diffusion equation that describes the flux of Li-ions under the influence of a concentration gradient $\nabla\zeta_+$ and an electric field $\nabla\phi$ [50]. We add the term $\frac{C_m^s}{C_0}\frac{\partial\xi}{\partial t}$ to the Nernst-Planck diffusion equation to account for the eliminated lithium ion from the electrolyte solution, due to electrodeposition on the solid phase (metal electrode). Thus, the diffusion equation becomes:

$$(9) \qquad \frac{\partial\widetilde{\zeta}_+}{\partial t} = \nabla \cdot \left(D^{\text{eff}}(\xi)\ \nabla\widetilde{\zeta}_+ + D^{\text{eff}}(\xi)\frac{nF}{RT}\widetilde{\zeta}_+\nabla\phi \right) - \frac{C_m^s}{C_0}\frac{\partial\xi}{\partial t},$$

where we interpolate the effective diffusivity by $D^{\text{eff}}(\xi) = D^s h(\xi) + D^l\left[1 - h(\xi)\right]$, with D^s and D^l as the electrode and electrolyte diffusivities, respectively.

2.3. **Electrostatic Potential.** We account for the electrostatic potential distribution ϕ using the charge continuity equation [56]

$$(10) \qquad \frac{\partial\rho}{\partial t} = -\nabla \cdot \vec{i},$$

where $\vec{i}$ is the current density and $\rho = \Sigma_i n_i F\zeta_i$ is the charge density. Experimental observations support the assumption that space-charge effects do not affect the stability of electrodeposits [105]. Therefore, we ignore the effects of the double-layer structure and assume electroneutrality, that is,

$$\widetilde{\zeta}_+ = \widetilde{\zeta}_-,$$

where we use Ohm's law in the continuity equation, $\vec{i} = \sigma\vec{E}$, and σ is the conductivity and $\vec{E} = -\nabla\phi$ is the electric field. Thus, we arrive at a Poisson equation, including a source term to represent the charges that enter or leave the system due to the electrochemical reaction [64]

$$(11) \qquad \nabla \cdot \left[\sigma^{\text{eff}}(\xi) \ \nabla\phi \right] = nF \mathrm{C}_m^s \frac{\partial\xi}{\partial t} \ .$$

We interpolate the effective conductivity using

$$\sigma^{\text{eff}}(\xi) = \sigma^s h(\xi) + \sigma^l \left[1 - h(\xi) \right],$$

where σ^s and σ^l are the electrode and electrolyte phase conductivity, respectively.

We collect the system of equations that models the physical process in the following box.

Box 1: Dendrite growth model

Lithium-battery dendrite growth process based on phase-field theory. *Find* $\Xi = \left(\xi, \widetilde{\zeta}_+, \phi \right)$ *fulfilling*

$$
\begin{cases}
\dfrac{\partial\xi}{\partial t} = -L_\sigma \left[\dfrac{\partial g(\xi)}{\partial\xi} - \nabla\cdot(\kappa(\xi)\nabla\xi) \right] - L_\eta \dfrac{\partial h(\xi)}{\partial\xi} \left[e^{\left(\frac{(1-\alpha)nF\phi}{RT} \right)} - \widetilde{\zeta}_+ \, e^{\left(\frac{-\alpha nF\phi}{RT} \right)} \right], & \text{in } V \times I \\[3mm]
\dfrac{\partial\widetilde{\zeta}_+}{\partial t} = \nabla\cdot\left[D^{\text{eff}}(\xi) \ \nabla\widetilde{\zeta}_+ + D^{\text{eff}}(\xi) \dfrac{nF}{RT}\widetilde{\zeta}_+\nabla\phi \right] - \dfrac{\mathrm{C}_m^s}{C_0}\dfrac{\partial\xi}{\partial t}, & \text{in } V \times I \\[3mm]
nF\mathrm{C}_m^s\dfrac{\partial\xi}{\partial t} = \nabla\cdot\left[\sigma^{\text{eff}}(\xi) \ \nabla\phi \right], & \text{in } V \times I \\[2mm]
\xi = \xi_D, & \text{on } \partial V_D \times I \\[1mm]
\widetilde{\zeta}_+ = \widetilde{\zeta}_{+D}, & \text{on } \partial V_D \times I \\[1mm]
\phi = \phi_D, & \text{on } \partial V_D \times I \\[1mm]
\nabla\xi \cdot \boldsymbol{n} = 0, & \text{on } \partial V_N \times I \\[1mm]
\nabla\widetilde{\zeta}_+ \cdot \boldsymbol{n} = 0, & \text{on } \partial V_N \times I \\[1mm]
\nabla\phi \cdot \boldsymbol{n} = 0, & \text{on } \partial V_N \times I \\[1mm]
\xi(\boldsymbol{x}, t_0) = \xi_0, & \text{in } V \\[1mm]
\widetilde{\zeta}_+(\boldsymbol{x}, t_0) = \widetilde{\zeta}_{+0}, & \text{in } V \\[1mm]
\phi(\boldsymbol{x}, t_0) = \phi_0, & \text{in } V
\end{cases}
$$

where V is the problem domain with boundary $\partial V = \partial V_N \cup \partial V_D$, the subscript N and D related to the Neumann and Dirichlet parts, with outward unit normal $\boldsymbol{n}$, and I is the time interval.

---

3. Weak variational formulation and space-time discretization

3.1. **Weak formulation.** We now state the weak variational formulation [106, 107] of the system of equations as: *Find* $\Xi = \left(\xi, \widetilde{\zeta}_+, \phi \right)$ *such that* $\forall V = (v, w, p)$

$$(12) \qquad \underbrace{\left\langle v, \dot{\xi} \right\rangle_V + \left\langle w, \dot{\widetilde{\zeta}}_+ \right\rangle_V + \left\langle w, \frac{\mathrm{C}_m^s}{C_0}\dot{\xi} \right\rangle_V + \left\langle p, \dot{\xi} \right\rangle_V}_{M\left(V, \dot{\Xi}\right)} = \underbrace{a\left(v, \xi, \widetilde{\zeta}_+, \phi \right) + b\left(w, \xi, \widetilde{\zeta}_+, \phi \right) + c\left(p, \xi, \phi \right)}_{A(V, \Xi)}$$

where $\dot{\bullet} = \frac{\partial \bullet}{\partial t}$ denotes the time derivative of the variable $\bullet = \xi, \widetilde{\zeta}_+$, $\langle u, w \rangle_V = \int_V wu \, dV$ expresses the inner product, and the functions on the right-hand side are

$$a(v, \Xi) = - \int_V L_\sigma \left[\frac{\partial g(\xi)}{\partial \xi} v + \kappa \nabla \xi \cdot \nabla v \right] dV - \int_V L_\eta \frac{\partial h(\xi)}{\partial \xi} \left[e^{\left(\frac{(1-\alpha)nF\phi}{RT} \right)} - \widetilde{\zeta}_+ \, e^{\left(\frac{-\alpha nF\phi}{RT} \right)} \right] v \, dV \ ,$$

$$(13) \qquad b(w, \Xi) = - \int_V \left[D^{\text{eff}}(\xi) \ \nabla \widetilde{\zeta}_+ \cdot \nabla w + D^{\text{eff}}(\xi) \frac{nF}{RT} \widetilde{\zeta}_+ \nabla \phi \cdot \nabla w \right] dV \ ,$$

$$c(p, \Xi) = - \frac{1}{nF C_m^s} \int_V \sigma^{\text{eff}}(\xi) \nabla \phi \cdot \nabla p \, dV.$$

We use standard finite element spaces where each function and its gradient are square integrable.

3.2. **Time semi-discretization.** We use a second-order backward-difference (BDF2) time marching scheme with an adaptive time step size. BDF2 is an implicit time marching method that requires the solution at two previous time instants; the initial step uses a first-order backward-difference method (BDF1). BDF2 has second-order accuracy and numerically damps the highest frequencies of the solution, unlike the conservative Crank-Nicolson method [106]. Liao et al. [108] showed that BDF2 is an effective time integrator for the phase-field crystal model, especially when coupled with an adaptive time-step strategy.

We discretize the time interval into $t_0 < t_1 < ... < t_n < ... < t_f$ and define the time-step size as $\Delta t_n = t_n - t_{n-1}$, approximate $\xi(t_n)$, $\dot{\xi}(t_n)$, $\widetilde{\zeta}_+(t_n)$ and $\dot{\widetilde{\zeta}}_+(t_n)$, respectively, as ξ_n, $\dot{\xi}_n$, $\widetilde{\zeta}_{+n}$ and $\dot{\widetilde{\zeta}}_{+n}$, and express the time increments as $\Delta \bullet = \bullet_{n+1} - \bullet_n$ for $\bullet = \xi, \dot{\xi}, \widetilde{\zeta}_+, \dot{\widetilde{\zeta}}_+$. We use a second-order approximation of the time derivative at t_{n+1} as follows [109],

$$(14) \quad \frac{\partial \bullet_{n+1}}{\partial t} = \left(\frac{1 + 2\omega_{n+1}}{1 + \omega_{n+1}} \right) \frac{\bullet_{n+1} - \frac{(1+\omega_{n+1})^2}{1 + 2\omega_{n+1}} \bullet_n + \frac{\omega_{n+1}^2}{1 + 2\omega_{n+1}} \bullet_{n-1}}{\Delta t_{n+1}}, \quad \text{with} \quad \omega_{n+1} = \frac{\Delta t_{n+1}}{\Delta t_n}, \quad \text{and} \quad \bullet = \xi, \widetilde{\zeta}_+ \ .$$

Then using this definition and letting $V_v = (v, 0, 0)$, we define the ξ-residual as

$$0 = R_\xi(V_v, \Xi_{n+1}) = M\left(V_v, \dot{\Xi}_{n+1} \right) - A(V_v, \Xi_{n+1})$$

$$(15) \qquad\qquad = \langle v, \xi_{n+1} \rangle_V + \underbrace{\left\langle v, \frac{(1+\omega_{n+1})^2}{1 + 2\omega_{n+1}} \xi_n - \frac{\omega_{n+1}^2}{1 + 2\omega_{n+1}} \xi_{n-1} \right\rangle_V}_{\ell_\xi(v) \ (\text{known at } t_n)} - \beta_{n+1} \Delta t_{n+1} \, a(v, , \Xi_{n+1})$$

with $\beta_{n+1} = \frac{1 + \omega_{n+1}}{1 + 2\omega_{n+1}}$. We now approximate $a(v, \Xi_{n+1})$ as a Taylor series expansion from Ξ_n to obtain

$$(16) \qquad a(v, \Xi_{n+1}) = a(v, \Xi_n) + a'_\xi(v, \Delta \xi; \Xi_n) + a'_{\widetilde{\zeta}_+}\left(v, \Delta \widetilde{\zeta}_+; \Xi_n \right) + \ a'_\phi(v, \Delta \phi; \Xi_n) + \mathcal{O}\left(\Delta t_{n+1}^2 \right)$$

where $\mathcal{O}(\Delta^2)$ represents neglected higher-order terms in the expansion and

$$(17) \qquad\qquad\qquad f'_\bullet(v, \Delta \bullet; \bullet_n) = \frac{d}{d\epsilon} \, f(v, \bullet_n + \epsilon \Delta \bullet)|_{\epsilon=0}$$

represents the directional Gâteaux derivative of the functional f in the direction $\bullet$. Combining (15) and (16), we obtain a linear equation system to solve, that is

$$(18) \qquad 0 = R_\xi(V_v, \Xi_n) + \langle v, \Delta \xi \rangle_V + \beta_{n+1} \Delta t_{n+1} \left[a'_\xi(v, \Delta \xi; \Xi_n) + a'_{\widetilde{\zeta}_+}\left(v, \Delta \widetilde{\zeta}_+; \Xi_n \right) + \ a'_\phi(v, \Delta \phi; \Xi_n) \right]$$

Similarly, we define the weighting functions $V_w = (0, w, 0)$ and $V_p = (0, 0, p)$; the residuals $\mathcal{R}_\bullet$ with $\bullet = \widetilde{\zeta}_+, \phi$ and linearize the resulting residuals to obtain the linearized system of equations to update the Newton iteration. We collect the linearized system of equations that models the physical process in the following box.

Box 2: Linearized equation system

Discrete linearized equations for lithium-battery dendrite growth process based on phase-field theory.

$Find\ \Xi_{n+1} = \left(\xi_n, \widetilde{\zeta}_{+n}, \phi_n\right) + \left(\Delta\xi, \Delta\phi, \Delta\widetilde{\zeta}_+\right)\ \ such\ that$

(19)
$$
\begin{cases}
0 = R_\xi\left(V_v, \Xi_n\right) + \langle v, \Delta\xi\rangle_V \\
\qquad + \beta_{n+1}\Delta t_{n+1}\left[a_\xi'\left(v, \Delta\xi; \Xi_n\right) + a_{\widetilde{\zeta}_+}'\left(v, \Delta\widetilde{\zeta}_+; \Xi_n\right) + a_\phi'\left(v, \Delta\phi; \Xi_n\right)\right] \\
0 = \mathcal{R}_{\widetilde{\zeta}_+}\left(V_w, \Xi_n\right) + \left\langle w, \Delta\widetilde{\zeta}_+ + \dfrac{C_m^s}{C_0}\Delta\xi\right\rangle_V \\
\qquad + \beta_{n+1}\Delta t_{n+1}\left[b_\xi'\left(w, \Delta\xi; \Xi_n\right) + b_{\widetilde{\zeta}_+}'\left(w, \Delta\widetilde{\zeta}_+; \Xi_n\right) + b_\phi'\left(w, \Delta\phi; \Xi_n\right)\right] \\
0 = \mathcal{R}_\phi\left(V_p, \Xi_n\right) + \langle p, \Delta\xi\rangle_V + \beta_{n+1}\Delta t_{n+1}\left[c_\xi'\left(p, \Delta\xi; \Xi_n\right) + c_\phi'\left(p, \Delta\phi; \Xi_n\right)\right]
\end{cases}
$$

We only expand c in the directions $\Delta\xi$ and $\Delta\phi$ as it is independent of $\Delta\widetilde{\zeta}_+$, see (13)$_3$.

For completeness, we summarize the Gâteaux derivatives in (19) in the following box.

Box 3: Gâteaux derivatives

(20)
$$
a_\xi'\left(v, \Delta\xi; \Xi_n\right) = \int_V L_\sigma\left[\left.\frac{\partial g^2(\xi)}{\partial \xi^2}\right|_{\xi_n}\Delta\xi\ v + \left(\kappa(\xi_n)\nabla\Delta\xi + \left.\frac{\partial\kappa(\xi)}{\partial\xi}\right|_{\xi_n}\Delta\xi\ \nabla\xi_n\right)\cdot\nabla v\right]dV
$$
$$
+ \int_V L_\eta\left.\frac{\partial h^2(\xi)}{\partial\xi^2}\right|_{\xi_n}\left[e^{\left(\frac{(1-\alpha)nF\phi_n}{RT}\right)} - \widetilde{\zeta}_{+n}\ e^{\left(\frac{-\alpha nF\phi_n}{RT}\right)}\right]\Delta\xi\ v\ dV
$$
$$
a_{\widetilde{\zeta}_+}'\left(v, \Delta\widetilde{\zeta}_+; \Xi_n\right) = \int_V L_\eta\left.\frac{\partial h(\xi)}{\partial\xi}\right|_{\xi_n}e^{\left(\frac{-\alpha nF\phi_n}{RT}\right)}\Delta\widetilde{\zeta}_+ v\ dV
$$
$$
a_\phi'\left(v, \Delta\phi; \Xi_n\right) = \int_V L_\eta\left.\frac{\partial h(\xi)}{\partial\xi}\right|_{\xi_n}\frac{nF}{RT}\left[(1-\alpha)e^{\left(\frac{(1-\alpha)nF\phi_n}{RT}\right)} + \alpha\widetilde{\zeta}_{+n}\ e^{\left(\frac{-\alpha nF\phi_n}{RT}\right)}\right]\Delta\phi\ v\ dV
$$
$$
b_\xi'\left(w, \Delta\xi; \Xi_n\right) = \int_V \left.\frac{\partial D^{\mathrm{eff}}(\xi)}{\partial\xi}\right|_{\xi_n}\Delta\xi\ \left(\nabla\widetilde{\zeta}_{+n} + \frac{nF}{RT}\ \widetilde{\zeta}_{+n}\nabla\phi_n\right)\cdot\nabla w\ dV
$$
$$
b_{\widetilde{\zeta}_+}'\left(w, \Delta\widetilde{\zeta}_+; \Xi_n\right) = \int_V D^{\mathrm{eff}}(\xi_n)\left(\nabla\Delta\widetilde{\zeta}_+ + \frac{nF}{RT}\Delta\widetilde{\zeta}_+\nabla\phi_n\right)\cdot\nabla w\ dV
$$
$$
b_\phi'\left(w, \Delta\phi, \Xi_n\right) = \int_V D^{\mathrm{eff}}(\xi_n)\frac{nF}{RT}\widetilde{\zeta}_{+n}\nabla\Delta\phi\cdot\nabla w\ dV
$$
$$
c_\xi'\left(p, \Delta\xi; \Xi_n\right) = \frac{1}{nFC_m^s}\int_V \left.\frac{\partial\sigma^{\mathrm{eff}}(\xi)}{\partial\xi}\right|_{\xi_n}\Delta\xi\ \nabla\phi_n\cdot\nabla p\ dV
$$
$$
c_\phi'\left(p, \Delta\phi; \Xi_n\right) = \frac{1}{nFC_m^s}\int_V \sigma^{\mathrm{eff}}(\xi_n)\nabla\Delta\phi\cdot\nabla p\ dV
$$

3.3. Space discretization.

We discretize the domain $V \subset \mathbb{R}^3$ with Dirichlet boundary condition ∂V_D and Neumann boundary condition ∂V_N using finite elements. We express the domain as the union of non-overlapping elements, K_i; thus, $V_h = \bigcup_{i=1}^M K_i$. We define continous piecewise polynomial functions over the discrete domain. In particular, we use linear functions over simplexes (i.e., triangles in 2D, tetrahedra in 3D).

Since the three variables share the spatial distribution of the boundary conditions, we use the shape functions $N_A(\boldsymbol{x})$ for each degree of freedom $\bullet_A^n$ at t_n satisfying the Dirichlet boundary conditions to discretize each degree of freedom $\bullet = X, Z, Y$ corresponding to the variables $\xi, \widetilde{\zeta}_+, \phi$, respectively; thus, we have

$$
(21) \qquad
\begin{aligned}
\xi_n^h &= \sum_{i=1}^{S} N_A(\boldsymbol{x}) X_A^n & \widetilde{\zeta}_{+n}^h &= \sum_{i=1}^{S} N_A(\boldsymbol{x}) Z_A^n & \phi_n^h &= \sum_{i=1}^{S} N_A(\boldsymbol{x}) Y_A^n \\
\Delta\xi^h &= \sum_{i=1}^{S} N_A(\boldsymbol{x}) \Delta X_A & \Delta\widetilde{\zeta}_+^h &= \sum_{i=1}^{S} N_A(\boldsymbol{x}) \Delta Z_A & \Delta\phi^h &= \sum_{i=1}^{S} N_A(\boldsymbol{x}) \Delta Y_A
\end{aligned}
$$

where S corresponds to the total number of unknowns in each solution variable. We define the weighting spaces using test spaces using the same functions but restricting those with support on ∂V_D to be zero, thus

$$
(22) \qquad v^h \in \text{span}\, \{N_B\}_{B=1}^{W} \quad w^h \in \text{span}\, \{N_B\}_{B=1}^{W} \quad p^h \in \text{span}\, \{N_B\}_{B=1}^{W}
$$

where W corresponds to the total number of weighting functions for each variable.

Using these spatial discretizations, we obtain the fully discrete algebraic problem:

$$
(23) \qquad
\underbrace{\left\{ \begin{array}{c} \Delta\mathcal{R}_\xi \\ \Delta\mathcal{R}_{\widetilde{\zeta}_+} \\ \Delta\mathcal{R}_\phi \end{array} \right\}}_{\Delta\mathcal{R}}
= \underbrace{\left(\begin{bmatrix} \mathbb{M}_{\xi\xi} & \mathbf{0} & \mathbf{0} \\ \mathbb{M}_{\widetilde{\zeta}_+\xi} & \mathbb{M}_{\widetilde{\zeta}_+\widetilde{\zeta}_+} & \mathbf{0} \\ \mathbb{M}_{\phi\xi} & \mathbf{0} & \mathbf{0} \end{bmatrix} + \beta_{n+1}\Delta t \begin{bmatrix} \mathbb{K}_{\xi\xi} & \mathbb{K}_{\xi\widetilde{\zeta}_+} & \mathbb{K}_{\xi\phi} \\ \mathbb{K}_{\widetilde{\zeta}_+\xi} & \mathbb{K}_{\widetilde{\zeta}_+\widetilde{\zeta}_+} & \mathbb{K}_{\widetilde{\zeta}_+\phi} \\ \mathbb{K}_{\phi\xi} & \mathbf{0} & \mathbb{K}_{\phi\phi} \end{bmatrix} \right)}_{\mathbb{J}} \cdot \underbrace{\left\{ \begin{array}{c} \Delta\boldsymbol{X} \\ \Delta\boldsymbol{Z} \\ \Delta\boldsymbol{Y} \end{array} \right\}}_{\Delta\boldsymbol{X}} .
$$

Box 4: Matrix blocks

The mass matrix blocks are

$$(24) \qquad \mathbb{M}_{AB}^{\xi\xi} = \mathbb{M}_{AB}^{\widetilde{\zeta}_+\widetilde{\zeta}_+} = \mathbb{M}_{AB}^{\phi\xi} = \sum_{k=1}^{M} \int_{K_k} N_A N_B \, dK_k \quad \text{and} \quad \mathbb{M}_{AB}^{\widetilde{\zeta}_+\xi} = \sum_{k=1}^{M} \int_{K_k} \frac{\mathrm{C}_m^s}{C_0} N_A N_B \, dK_k$$

while stiffness matrix blocks are

$$(25) \quad \begin{cases} \mathbb{K}_{AB}^{\xi\xi} = \displaystyle\sum_{k=1}^{M} \int_{K_k} L_\sigma \left[\frac{\partial g^2}{\partial \xi^2}\bigg|_{\xi_n^h} N_A \, N_B + \left(\kappa\left(\xi_n^h\right) \nabla N_A + \frac{\partial \kappa}{\partial \xi}\bigg|_{\xi_n^h} N_A \, \nabla \xi_n^h \right) \cdot \nabla N_B \right] \, dK_k \\[3mm]
\qquad + \displaystyle\sum_{k=1}^{M} \int_{K_k} L_\eta \frac{\partial h^2}{\partial \xi^2}\bigg|_{\xi_n^h} \left[e^{\left(\frac{(1-\alpha)nF\phi_n^h}{RT}\right)} - \widetilde{\zeta}_{+n}^h \, e^{\left(\frac{-\alpha nF\phi_n^h}{RT}\right)} \right] N_A \, N_B \, dK_k \\[3mm]
\mathbb{K}_{AB}^{\xi\widetilde{\zeta}_+} = \displaystyle\sum_{k=1}^{M} \int_{K_k} L_\eta \frac{\partial h}{\partial \xi}\bigg|_{\xi_n^h} e^{\left(\frac{-\alpha nF\phi_n^h}{RT}\right)} N_A N_B \, dK_k \\[3mm]
\mathbb{K}_{\xi\phi} = \displaystyle\sum_{k=1}^{M} \int_{K_k} L_\eta \frac{\partial h}{\partial \xi}\bigg|_{\xi_n^h} \frac{nF}{RT} \left[(1-\alpha) \, e^{\left(\frac{(1-\alpha)nF\phi_n^h}{RT}\right)} + \alpha \widetilde{\zeta}_{+n}^h \, e^{\left(\frac{-\alpha nF\phi_n^h}{RT}\right)} \right] N_A \, N_B \, dK_k \\[3mm]
\mathbb{K}_{AB}^{\widetilde{\zeta}_+\xi} = \displaystyle\sum_{k=1}^{M} \int_{K_k} \frac{\partial D^{\mathrm{eff}}}{\partial \xi}\bigg|_{\xi_n^h} N_A \left[\nabla \widetilde{\zeta}_{+n}^h + \frac{nF}{RT} \, \widetilde{\zeta}_{+n}^h \nabla \phi_n^h \right] \cdot \nabla N_B \, dK_k \\[3mm]
\mathbb{K}_{\widetilde{\zeta}_+\widetilde{\zeta}_+} = \displaystyle\sum_{k=1}^{M} \int_{K_k} D^{\mathrm{eff}}\left(\xi_n^h\right) \left[\nabla N_A + \frac{nF}{RT} N_A \nabla \phi_n^h \right] \cdot \nabla N_B \, dK_k \\[3mm]
\mathbb{K}_{AB}^{\widetilde{\zeta}_+\phi} = \displaystyle\sum_{k=1}^{M} \int_{K_k} D^{\mathrm{eff}}\left(\xi_n^h\right) \frac{nF}{RT} \, \widetilde{\zeta}_{+n}^h \, \nabla \mathrm{N}_A \cdot \nabla N_B \, dK_k \\[3mm]
\mathbb{K}_{AB}^{\phi\xi} = \dfrac{1}{nF\mathrm{C}_m^s} \displaystyle\sum_{k=1}^{M} \int_{K_k} \frac{\partial \sigma^{\mathrm{eff}}}{\partial \xi}\bigg|_{\xi_n^h} N_A \, \nabla \phi_n^h \cdot \nabla N_B \, dK_k \\[3mm]
\mathbb{K}_{AB}^{\phi\phi} = \dfrac{1}{nF\mathrm{C}_m^s} \displaystyle\sum_{k=1}^{M} \int_{K_k} \sigma^{\mathrm{eff}}\left(\xi_n^h\right) \, \nabla N_A \cdot \nabla N_B \, dK_k \end{cases}$$

4. Time-adaptive strategy

Time step adaptivity is highly useful in this problem, where the time step requirements vary significantly at different simulation stages. For example, initially, the simulation requires small time steps to achieve convergence during the development of the phase-field interface and thereon, their size grows a few orders of magnitude (i.e., from $\Delta t = 10^{-6} \, [s]$ up to $\Delta t = 10^{-1} \, [s]$) depending on the parameters (e.g., mesh size, electrodeposition rate).

Following [110, 111], we express the local truncation error for BDF2 using Taylor expansions as follows

$$(26) \qquad \tau^{\mathrm{BDF2}}\left(t_{n+1}\right) = \frac{\Delta t_{n+1}^2 \left(\Delta t_n + \Delta t_{n-1}\right)}{6} \dddot{u}\left(t_{n+1}\right) + \mathcal{O}\left(\Delta t^4\right) \;,$$

where $u = \xi, \widetilde{\zeta}_+$, since ϕ's time derivative does not appear explicitly in the formulation. We use the solutions u_{n+1}, u_n, u_{n-1} and u_{n-2} from the BDF2 scheme to estimate the truncation error of (26) using the third-order backward difference formula (BDF3)

$$(27) \qquad \dddot{u}\left(t_{n+1}\right) \approx \frac{1}{\Delta t_{n+1}^2} \left[\frac{u_{n+1} - u_n}{\Delta t_{n+1}} - \left(1 + \frac{\Delta t_{n+1}}{\Delta t_n}\right) \frac{u_n - u_{n-1}}{\Delta t_n} + \frac{\Delta t_{n+1}}{\Delta t_n \Delta t_{n-1}} \left(u_{n-1} - u_{n-2}\right) \right].$$

Thus, we estimate BDF2's local truncation error by substituting (27) into (26) to obtain

$$(28) \quad \tau^{\mathrm{BDF2}}\left(t_{n+1}\right) \approx \frac{\Delta t_n + \Delta t_{n-1}}{6} \left[\frac{u_{n+1} - u_n}{\Delta t_{n+1}} - \left(1 + \frac{\Delta t_{n+1}}{\Delta t_n}\right) \frac{u_n - u_{n-1}}{\Delta t_n} + \frac{\Delta t_{n+1}}{\Delta t_n \Delta t_{n-1}} \left(u_{n-1} - u_{n-2}\right) \right],$$

Finally, we compute the weighted local truncation error as an error indicator [112]

$$(29) \qquad E_u\left(t_{n+1}\right) = \sqrt{\frac{1}{N} \sum_{i=1}^{N} \left(\frac{\tau_i^{\mathrm{BDF2}}\left(t_{n+1}\right)}{\rho_{abs} + \rho_{rel} \max\left(|u_{n+1}|_i, |u_{n+1}|_i + |\tau^{\mathrm{BDF2}}\left(t_{n+1}\right)|_i\right)} \right)^2},$$

where ρ_{abs} and ρ_{rel} are user-defined parameters that define the absolute and relative tolerances, respectively. In our examples we set these parameters to $\rho_{abs} = \rho_{rel} = 10^2$. The time error is computed using the maximum time error of time-dependent variables

$$(30) \qquad E\left(t_{n+1}\right) = \max\left(E_\xi\left(t_{n+1}\right), E_{\widetilde{\zeta}_+}\left(t_{n+1}\right)\right),$$

and the time-step adaptivity simply follows [113, 114]

$$(31) \qquad \Delta t_{n+1}^{k+1}\left(t_{n+1}\right) = \boldsymbol{F}\left(E\left(t_{n+1}\right), \Delta t_{n+1}^k, \mathrm{tol}\right) = \rho_{tol} \left(\frac{\mathrm{tol}}{E\left(t_{n+1}\right)}\right)^{\frac{1}{2}} \Delta t_{n+1}^k,$$

where k is the time-step refinement level and ρ_{tol} is a safety factor parameter set to 0.9 in our simulations. We summarize the time-adaptive scheme in Algorithm 1, where we define two tolerances tol_{max} and tol_{min} that limit the range of reduction or increments of the time-step size.

5. IMPLEMENTATION DETAILS

This section briefly discusses the implementation aspects and details the step-by-step calculations. We perform all the numerical experiments using the open-source FEniCS environment [115] using the FIAT package [116] to integrate numerically and assemble the matrices and vectors. We use four-node quadrilateral elements in 2D and eight-node hexahedral elements in 3D,; in all cases, we use consistent Gaussian quadrature. We use a passing interface package MPI4py [117–120] for parallelization and solve nonlinear using SNES combined with BiCGStab for each linear system, including a Nonlinear Additive Schwarz methods (NASM) for parallel solution [121]. Table 1 summarizes the parameters we use.

TABLE 1. Numerical parameters summarize

Description	Symbol	Value
Max. iteration number for SNES	$\mathrm{it}_{\max}$	8
Relative tolerance for SNES	tol	10^{-8}
Max. iteration number for Krylov	$\mathrm{it}_{\mathrm{Kr}}$	1000
Relative tolerance for Krylov	$\mathrm{tol}_{\mathrm{Kr}}$	10^{-22}
Max. tolerance for time-adaptive scheme	$\mathrm{tol}_{\max}$	10^{-5}
Min. tolerance for time-adaptive scheme	$\mathrm{tol}_{\min}$	10^{-7}
Safety factor for time-adaptive scheme	ρ_{tol}	0.9
Relative scale factor for time-error computation	ρ_{rel}	10^2
Absolute scale factor for time-error computation	ρ_{abs}	10^2

We compute the time increment by gathering the unknown vectors at the master core, estimating the error for the current time step, adapting the time step size, and broadcasting its value to the other cores. This straightforward implementation is practical given the small number of processors used. We initialize the simulations using a first-order backward difference formula (BDF1) until $\bullet_{n-2}$ is different from null. We perform the simulations using a laptop with a 2.4 GHz processor with 8-core Intel Core i9 and 16 GB 2667 MHz DDR4 RAM, obtaining satisfactory results using a regular computer. Algorithm 1 sketches the time marching scheme, where $rank$ is the core number, and $master$ is the master core used as the communicator.

Algorithm 1: Dendrite growth model based on phase-field theory with time adaptivity

---

Data: $\bullet_n$, $\bullet_{n-1}$, $\bullet_{n-2}$, $\dot{\bullet}_n$, Δt_{n+1}, Δt_n, Δt_{n-1}
Result: updated variables $\bullet_{n+1}$, $\dot{\bullet}_{n+1}$, Δt_{n+1}

1 Initialize $\bullet_n = \bullet_0$, with $\bullet = \xi, \widetilde{\zeta}_+, \phi$;
2 **while** $t_{n+1} \leq t_f$ **do**
3   Solve non-linear problem (23) ;
4   Gather $\Delta \boldsymbol{X}$ in master core and calculate temporal error $\tau^{\mathrm{BDF2}}\left(t_n + \Delta t_{n+1}\right)$ with (28) ;
5   **if** *rank == master* **then**
6   Calculate $E_u\left(t_n + \Delta t_{n+1}\right)$ with (29) ;
7   Take the maximum error with (30) ;
8   **if** $E\left(t_n + \Delta t_{n+1}\right) \leq tol_{max}$ **then**
9   Update current time step $t_{n+1} \leftarrow t_n + \Delta t_{n+1}$;
10   Update $\bullet_{n+1}$ and $\dot{\bullet}_{n+1}$;
11   Update $\bullet_{n-2} \leftarrow \bullet_{n-1}$, $\bullet_{n-1} \leftarrow \bullet_n$, $\bullet_n \leftarrow \bullet_{n+1}$ and $\dot{\bullet}_n \leftarrow \dot{\bullet}_{n+1}$;
12   **if** $E\left(t_n + \Delta t_{n+1}\right) < tol_{min}$ **then**
13   Increase delta step for next time increment $\Delta t_{n+1} \leftarrow \boldsymbol{F}\left(E\left(t_{n+1}\right), \Delta t_{n+1}, \mathrm{tol}_{\min}\right)$
                         using (31) ;
14   **end**
15   Broadcast to rest of ranks all variables Δt_{n+1}, $\bullet_{n-2}$, $\bullet_{n-1}$ and $\bullet_n$;
16   **else**
17   Reduce time-step size$\Delta t_{n+1} \leftarrow \boldsymbol{F}\left(E\left(t_{n+1}\right), \Delta t_{n+1}, \mathrm{tol}_{\max}\right)$ using (31) ;
18   Broadcast to rest of ranks only Δt_{n+1} ;
19   **end**
20   **end**
21 **end**

---

6. Simulations of lithium-metal dendrite formation

We present several studies that evaluate the performance of the proposed electrodeposition model for metal anode battery simulations. These studies consist of 2D and 3D simulations of dendritic electrodeposition of lithium metal during battery charge status.

6.1. **System layout and properties.** Generally, the computational domain for a battery simulation comprises the anode and cathode regions as well as the space between the electrodes filled with electrolyte [122]. However, in most phase-field simulations of metal electrodeposition, including those we perform, the cathode region reduces to a current collector boundary condition on the electrolyte side of the domain (see Figure 2). We model a battery cell with a traditional sandwich architecture, undergoing a recharging process under fixed applied electro potential. We represent this cell as an $l_x \times l_y$ rectangular domain in 2D and as an $l_x \times l_y \times l_z$ hexagonal domain in 3D. The initial perturbation (dendrite nuclei) significantly impacts the simulation outcome. These nuclei are usually part of the problem's initial conditions. Some models include initial seeds (artificial deformation on the electrode surface) combined with surface anisotropy to propagate the dendrite shape [45, 58, 61]. Alternatively, other models combine surface anisotropy with Langevin noise at the phase-field interface to generate a random nucleation pattern [65, 67, 68, 77]. In our experience, the shape of the initial seed and the noise levels have a major influence on the resulting dendrite morphology.

We study two different initial structures. The first structure consists of a $5 \mu m$-thick metal anode ($l_0 = 5\,[\mu m]$), made up of pure Lithium, separated from the liquid electrolyte by a smooth interface, as Figure 2-a depicts. The initial condition drives from the equilibrium solution for a one-dimensional transition zone between solid ($\xi = 1$) and liquid ($\xi = 0$), where our variables $\left(\xi, \widetilde{\zeta}_+, \phi\right)$ vary in the "x" spatial direction according to $\xi\left(x\right) = \frac{1}{2}\left[1 - \tanh\left(x\sqrt{\frac{W}{2\kappa_0}}\right)\right]$ [104].

In the second structure we assume that artificial nucleation regions, ellipsoidal protrusions (seeds) with semi-axes r_x, r_y, r_z, and center $\left(l_{0_x}, l_{0_y}, l_{0_z}\right)$, exist at the surface of the anode undergoing electrodeposition (see Figure 2-b). This is a widely-used strategy in phase-field simulations of electrodeposition [63, 64, 67, 68]; since it reduces the computational cost as the lithium metal is only able to electrodeposit on the same nuclei, enhancing dendrite growth and allowing for detailed study of its morphology. For the artificial nucleation case, we modify the initial condition formula, replacing "x" by $\left[\left(\frac{x-l_{0_x}}{r_x}\right)^2 + \left(\frac{y-l_{0_y}}{r_y}\right)^2 + \left(\frac{z-l_{0_z}}{r_z}\right)^2 - 1\right]$ within the hyperbolic tangent argument, to account for a smooth transition between the solid seed (lithium metal anode) and the surrounding liquid electrolyte region.

We assume the cell's electrolyte to be 1M LiPF$_6$ EC/DMC 1:1 volume ratio solution [66]; we compute the electrolyte's site density (C_m^l) using its density ($1.3\left[g/cm^3\right]$) and molar mass ($90\left[g/mol\right]$) and electrode's site density C_m^s using the density ($0.534\left[g/cm^3\right]$) and molar mass ($6.941\left[g/mol\right]$) of pure Lithium [66].

We model the anode boundary as a Dirichlet boundary condition $\xi = 1$ at $x = 0$ for the phase-field parameter (solid electrode phase). In contrast, we use a no-flux Neumann boundary condition at $x = l_x$ (cathode) to allow the electrodeposition process to take place (ξ changing from 0 to 1) when the reaction front approaches the short-circuit condition [95]. For the Li-ion concentration, we apply Dirichlet boundary conditions setting $\widetilde{\zeta}_+ = 0$ and $\widetilde{\zeta}_+ = 1$ at the anode ($x = 0$) and cathode ($x = l_x$) boundaries, respectively. These boundary conditions allow the Li-ion flux into the battery (electrolyte side), ensuring that the Li deposited at the electrode-electrolyte interface equals the amount of Li^+ supplied to the electrolyte. Thus, these boundary conditions avoid the quick Li-ion depletion and keep the electrodeposition process running for the full simulation [95]. Finally, we apply periodic boundary conditions on the remaining faces; these are $(x, 0, z)$, (x, l_y, z), $(x, y, 0)$, and (x, y, l_z). Figure 2 summarizes the boundary conditions we apply.

Additionally, Table 2 presents the phase-field model parameters. The normalization constants for length, time, energy and concentration scales are set as $h_0 = 1\,[\mu m]$, $t_0 = 1\,[s]$, $E_0 = 2.5 \times 10^6\left[J/m^3\right]$, and $C_0 = 1 \times 10^3\left[mol/m^3\right]$, respectively [66]. Table 2 also shows that although the electrode and electrolyte materials can exhibit Li/Li^+ dependent conductivities and diffusivities, their values are set to constants across each phase for simplicity [65, 66].

TABLE 2. Simulation Parameters

Description	Symbol	Real Value	Normalized	Source
Exc. current density	i$_0$	$30\left[A/m^2\right]$	30	[123]
Surface tension	γ	$0.556\left[J/m^2\right]$	0.22	[124, 125]
Phase-field interface thickness	δ_{PF}	$1.5 \times 10^{-6}\,[m]$	1.5	[95]
Barrier height	W	$W = \frac{12\gamma}{\delta_{PF}} = 4.45 \times 10^6\left[J/m^3\right]$	1.78	computed
Gradient energy coefficient	κ_0	$\kappa_0 = \frac{3\gamma\delta_{PF}}{2} = 1.25 \times 10^{-6}\,[J/m]$	0.5	computed
Anisotropy strength	δ_{aniso}	0.044	0.044	[97, 125]
Anisotropy mode	ω	4	4	[97, 98]
Kinetic coefficient	L_η	$L_\eta = i_0\frac{\gamma}{nFC_m^s} = 1.81 \times 10^{-3}\,[1/s]$	1.81×10^{-3}	computed
Site density electrode	C$_m^s$	$7.64 \times 10^4\left[mol/m^3\right]$	76.4	[66]
Bulk Li-ion concentration	C$_0$	$10^3\left[mol/m^3\right]$	1	computed
Conductivity electrode	σ^s	$10^7\,[S/m]$	10^7	[64]
Conductivity electrolyte	σ^l	$1.19\,[S/m]$	1.19	[126]
Diffusivity electrode	D^s	$7.5 \times 10^{-13}\left[m^2/s\right]$	0.75	[64]
Diffusivity electrolyte	D^l	$3.197 \times 10^{-10}\left[m^2/s\right]$	319.7	[126]

6.2. Lithium dendrite propagation rate: Consistency with experimental data.

Validation of phase-field models with experimental results is a well-known challenge of electrodeposition simulations [65]; partly due to the computational cost of simulating the detailed lithium electrodeposition at the whole-cell scale [67]. One limiting factor is the domain size, defined by the inter-electrode separation distance in experimental cells, which ranges from 1 to 10mm [94, 127, 128].

(A) Planar electrode.
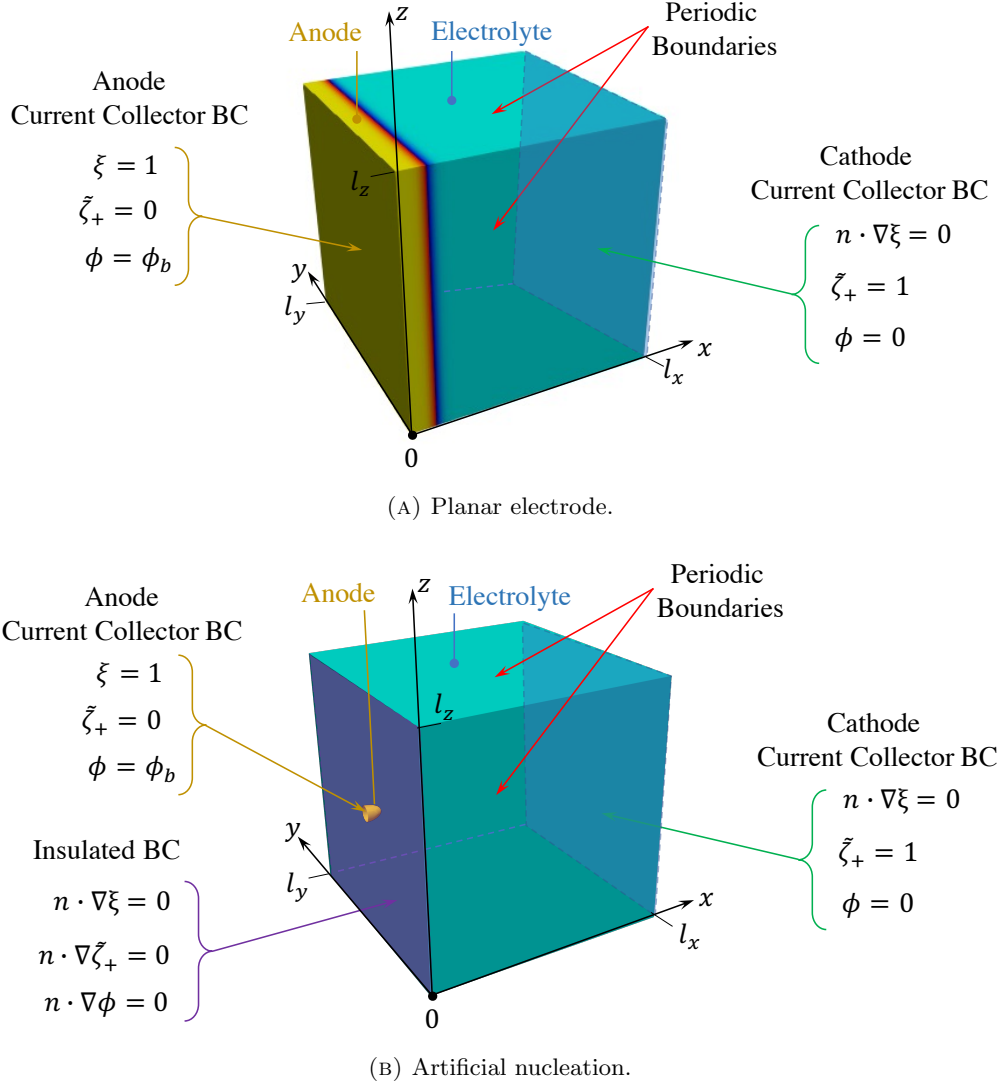

(B) Artificial nucleation.

FIGURE 2. Boundary conditions for planar electrode (a) and artificial nucleation (b) simulations.

We perform 2D simulations to directly compare our simulations against experimental results obtained from thin-cell geometries. We use 2D simulation results to validate the predicted lithium dendrite propagation rates, assuming that the electrodeposition rates are not significantly affected by the problem's size.

We achieve large simulation sizes through several computational efficiency improvements. We use a sigmoid interpolating function [95] instead of the popular polynomial interpolating function [61, 63, 64]. We use time-step size adaptivity and mesh mapping in the region of interest (close to the electrode-electrolyte interface). We also use parallel solution strategies and carefully select the phase-field interface thickness (δ_{PF}), given the interface thickness effect on the electrodeposition rate, which ultimately determines the evolution dynamics (motion) of the lithium electrodeposits [95].

We compare the simulated lithium dendrite propagation rate against the experimental measurements of Nishikawa et al. [94]. Nishikawa et al. studied the dendritic electrodeposition of lithium as a function of total charge (electric current passed over time) using microscope observations. They reported dendrite growth rates of $0.01 - 0.06 \left[\mu m s^{-1}\right]$ [37] using a 1M LiPF$_6$ electrolyte, establishing upper and lower bounds for comparison with our simulation results. The wide range of values reported in many studies [32, 94, 129] may be caused by the uneven current distribution on the electrode surface [94].

(A) $t = 0\,[s]$.

(B) $t = 400\,[s]$.

(C) $t = 800\,[s]$.
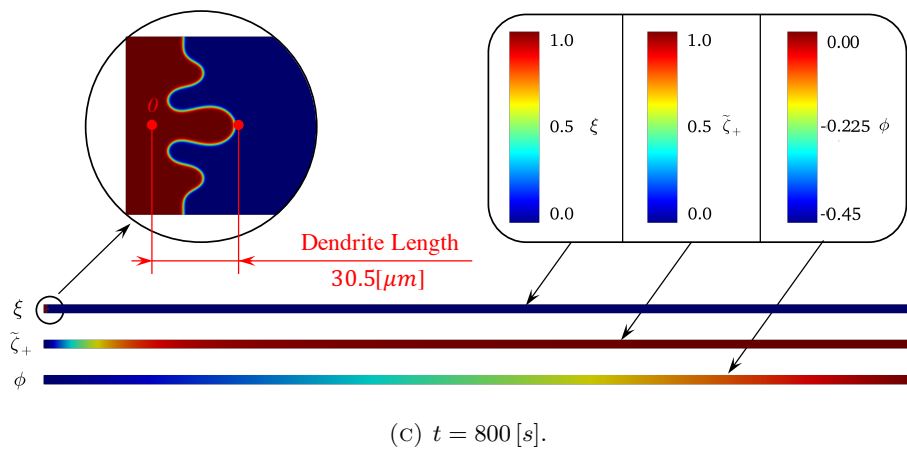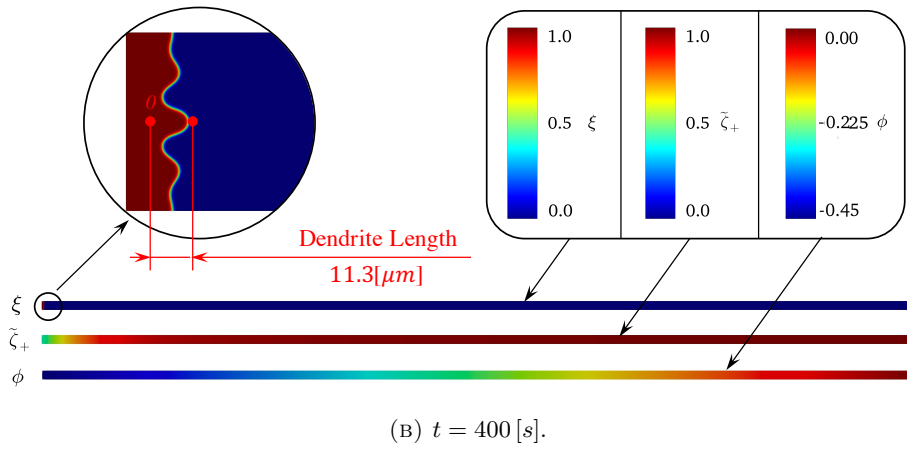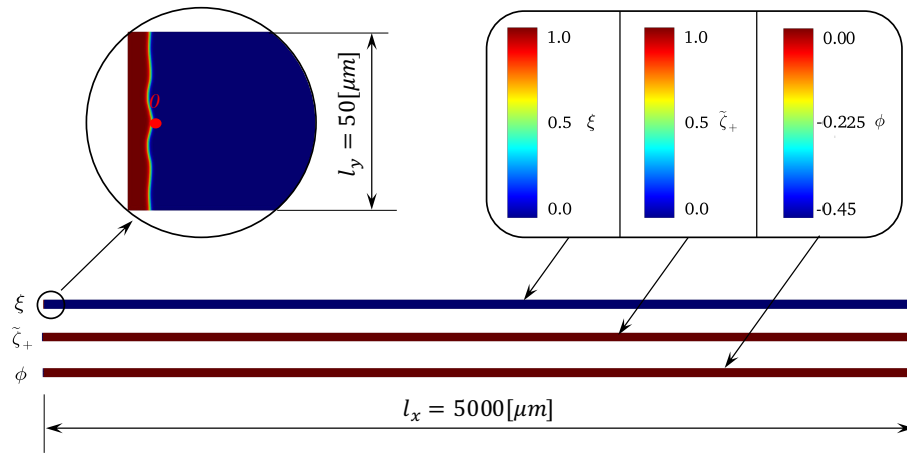
FIGURE 3. 2D phase-field simulation of lithium electrodeposition process at a current density of $i = 10\,[mA/cm^2]$ with a distance of $l_x = 5000\,[\mu m]$ between electrodes.

We simulate a lithium electrodeposition process at an applied current density of $i = 10 \left[mA/cm^2 \right]$ [94]. We use a 2D rectangular domain $l_x = 5000 \left[\mu m \right]$ long (distance betweenelectrodes), and $l_y = 50 \left[\mu m \right]$ wide (sufficient width to allow dendrite formation). We use a mesh $8,000 \times 140$ elements, with mesh distribution that guarantees an x-spatial resolution of approximately $0.35 \left[\mu m \right]$ ($h < 4\delta_{PF}$) in the region of interest of the domain with square elements. We apply a charging electro potential of $\phi_b = -0.45 \left[V \right]$ to the cell (a common value in the literature [64–66]), well above the threshold overpotential for dendrite growth $\phi_b = -0.37 \left[V \right]$ [66]. We perturb the initial electrode surface by ($\pm 0.5 \left[\mu m \right]$) in x-direction according to $0.4 \sin \left(0.44y + \pi \right) e^{-0.004(y-0.5l_y)^2}$, consisting of a periodic function combined with a Gaussian distribution to promote dendrite formation at the center of the domain ($\frac{l_y}{2} = 25 \left[\mu m \right]$).

Figure 3 shows the initial conditions ($t = 0 \left[s \right]$) and the evolution of the system's variables $\left(\xi, \widetilde{\zeta}_+, \phi \right)$. We zoom in the phase-field variable ξ at each instant to emphasize the growth of the lithium dendrite and show the instantaneous dendrite length measurement. Figure 4 shows the evolution of the simulated lithium dendrite length over time (blue). While in the range of experimental data (green), the results are sensitive to differences between the transport and kinetic properties and those of the experiments [94] and our simulator. Therefore, further well-controlled experimental studies, with detailed characterization of the system parameters, combined with modeling will be necessary to improve the correlation [37].
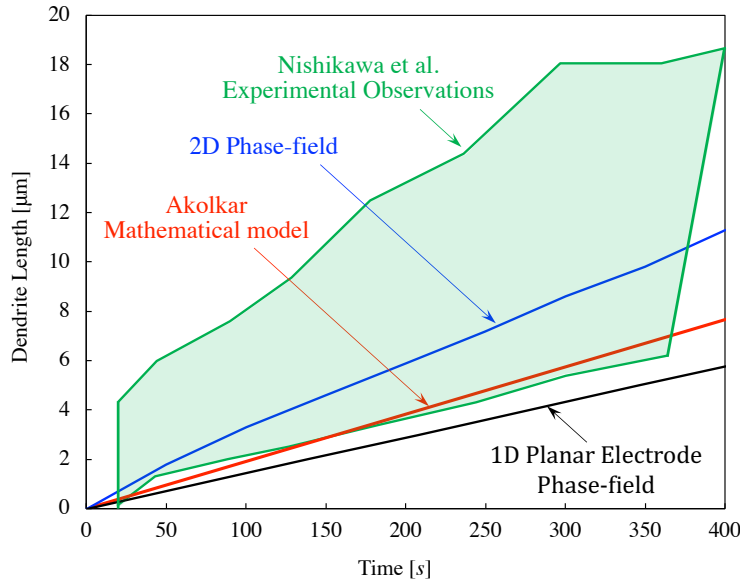
FIGURE 4. Comparison between 2D phase-field simulations of lithium dendrite growth at a current density of $i = 10 \left[mA/cm^2 \right]$ (blue), experimental data taken from Nishikawa et al. [94] (green), and the Akolkar analytical model predictions [37] (red). 1D planar electrode phase field simulation for reference (black).

Additionally, Figure 4 includes analytical dendrite propagation results for the tip current density developed by Akolkar [37] for comparison. Akolkar's model calculates the dendrite propagation rate by analyzing various overpotentials that develop at the dendrite tip and the flat electrode surface, assuming a current density of $i = 10 \left[mA/cm^2 \right]$ applied and a constant radius of $r = 1 \left[\mu m \right]$ at the dendrite's tip. This simplification constitutes departs from our phase-field model, where the dendrite's tip radius is variable throughout the simulation. This difference may partly explain the higher growth rate obtained in our simulations. Furthermore, we also include 1D planar electrode phase-field results using an identical set-up as to the 2D simulation [95].

6.3. **2D Simulation of lithium dendrite growth.** The following 2D numerical experiment compares our model's features to other phase-field simulations reported in the literature. This comparison verifies our

work as a preliminary step to continue with a series of larger and more complex 3D simulations of lithium dendrite growth in metal anode batteries latter in this paper.

In this case, we use a 2D square domain set as $360 \times 360 \left[\mu m^2\right]$, within the range of typical distances between electrodes in metal anode batteries [6]. We use a 500×720 structured mesh with a mapping in the x-direction to obtain square elements of size $0.5 \times 0.5 \left[\mu m^2\right]$ in the region of interest (see Section 6.4 for details). We apply a charging electro potential of $\phi_b = -0.7 \left[V\right]$ to the cell, with an artificial nucleation region with 3 protrusions (ellipsoidal seeds), equally spaced, growing from the left boundary, with semi-axes $4\left[\mu m\right] \times 1\left[\mu m\right]$. Figure 5 shows the evolution of our system's variables $\left(\xi, \widetilde{\zeta}_+, \phi\right)$ at different time steps. The corresponding temporal-spatial distribution of the phase-field variable ξ depicts the dynamic morphological evolution of the simulated lithium dendrite.

(A) $t = 5\,[s]$.   (B) $t = 20\,[s]$.   (C) $t = 50\,[s]$.   (D) $t = 70\,[s]$.
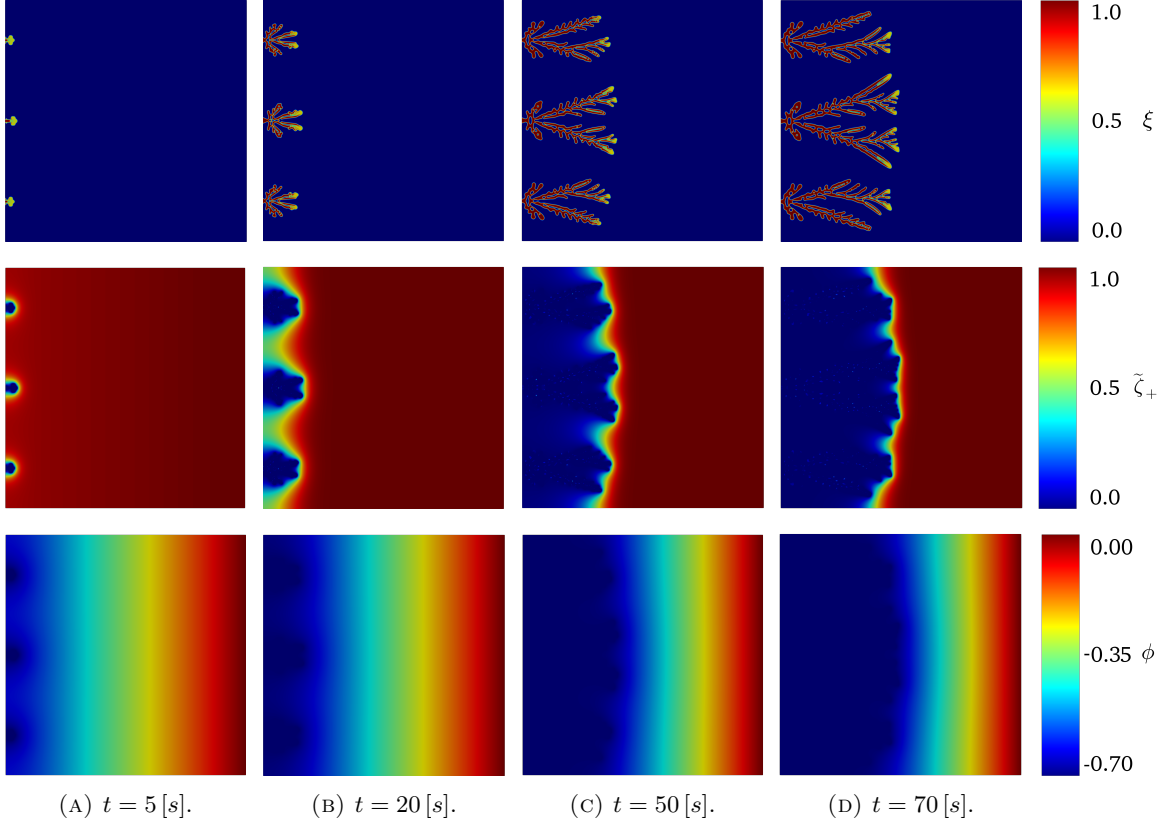
FIGURE 5. 2D phase-field simulation of bush-like lithium dendrite formation under $\phi_b = -0.7\,[V]$ charging potential. The upper row shows the lithium solid-phase evolution ξ; the second row shows the lithium-ion distribution $\widetilde{\zeta}_+$; and the third row shows the electric potential field ϕ. Square domain set as $360 \times 360 \left[\mu m^2\right]$.

Figure 5 shows the evolution of bush-like lithium dendrite formation, having morphological resemblance to the dendritic patterns reported in previous phase-field studies of dendrite growth [67, 75]. The lithium dendrites grow from each nucleation site and move towards the opposite electrode, following the electric field $(\vec{E} = -\nabla\phi)$. As the dendrite grows, side branches appear, growing across the electrolyte, in agreement with lithium dendrite experiments [42]. The computed width range of lithium branches is between 5 and 13 $[\mu m]$. These bush-like morphologies grow fast across the electrolyte region and penetrate through porous separators, becoming potentially dangerous as they can produce battery short circuits [6]. The spatial distribution of the lithium-ion concentration $\widetilde{\zeta}_+$, and electric potential ϕ, corresponding to the second and third rows of Figure 5 respectively, show that they follow the same trend reported in other phase-field models of lithium dendrite growth [61, 67]. The lithium-ion concentration remains equal to the bulk concentration, $\widetilde{\zeta}_+ = 1$, through the electrolyte phase and decreases near the dendrite front (solid phase) due to the electrodeposition

process [64]. The electric potential has a large gradient that spreads over the electrolyte phase and remains constant and equal to ϕ_b at the electrode phase. As the lithium dendrite moves across the electrolyte region, the gradient of the electric potential (electric field) increases, in agreement with simulation results reported by Hong et al. [61].
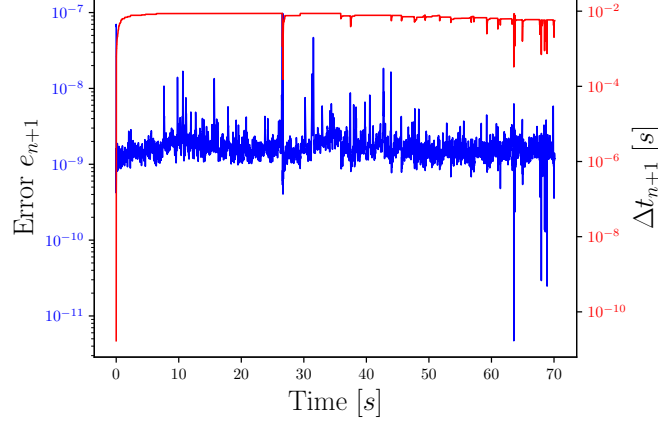

FIGURE 6. Performance of time-adaptive strategy in 2D lithium dendrite growth simulation. Weighted local truncation error (blue) and time-step size (red) vs time.

Figure 6 illustrates the interplay between the weighted truncation error estimate e_{n+1} (30) (blue) and the time-step size evolution Δt_{n+1} (31) (red), throughout the $70\,[s]$ of simulation. The figure shows that the simulation initially requires a small time-step size of $\Delta t_0 = 10^{-10}\,[s]$ to converge as the phase field develops its interface thickness and the ion concentration and electro potential distributions achieve equilibrium. The time-step size increases sharply, achieving a stationary size of $\Delta t_{n+1} = 10^{-2}\,[s]$, after $5\,[s]$ of simulation. In addition, the time-step size starts to decrease slightly after $40\,[s]$, which corresponds with the acceleration of lithium dendrite propagation rate as it approaches the opposite electrode [61]. The maximum and minimum tolerances for the time-adaptive scheme are 10^{-7} and 10^{-9} in this case, allowing the time-step size to decrease or increase accordingly when error tolerances bounds are reached.

(A) 3D mesh partition in 8 processors.   (B) Simple nucleation.
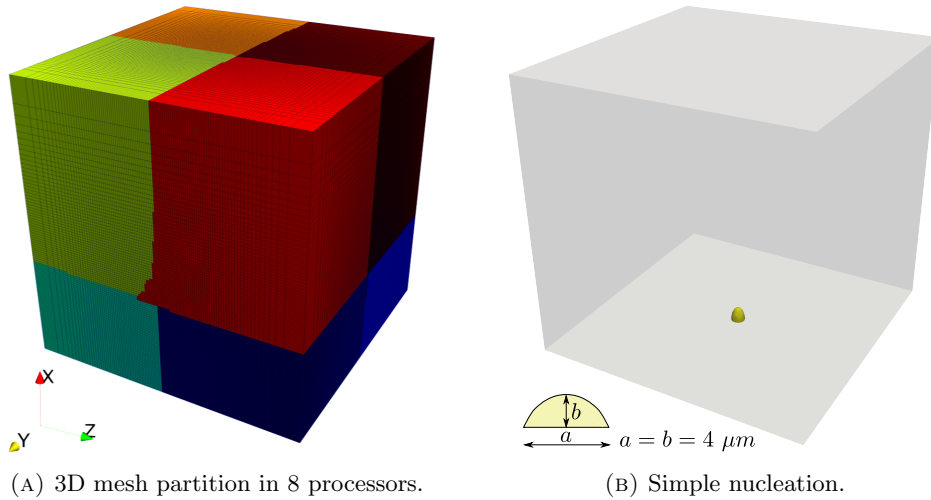
FIGURE 7. 3D mesh partition in 8 processors, each one represented by a different color (a), and geometry of the initial protrusion for the simple nucleation experiment (b).

6.4. **3D simulation of lithium dendrite growth: Single nucleus experiment.** This section describes 3D phase-field simulations of lithium dendrite formation to study three-dimensional highly branched "spike-like" dendritic patterns, commonly observed experimentally. These patterns form under high current density loads, which correspond to fast battery charge [69, 83, 84]. We select a geometrical unit that characterizes a real cell structure [67, 122]. We choose a computational domain of $80 \times 80 \times 80 \left[\mu m^3\right]$. Consequently, given the domain size, we expect growth rates up-to two orders of magnitude faster-than-normal, due to the short separation between electrodes $l_x = 80\,[\mu m]$.

We use a 3D structured mesh with eight-node hexahedral elements. We distribute the mesh to focus the node's mapping on the area of interest (see Figure 7a). In particular, in the x-direction $x_r = (2/\pi)\,arcsin(x_u)$; where x_u is the node's x coordinate normalized by l_x, before mapping (uniform distribution), and x_r is the node's mapped coordinate. The arcsin function transitions smoothly, inducing a relatively small variation in the mesh size within 50% of the physical domain where the lithium electrodeposit process occurs [67, 68, 76]. The mapping produces a finer mesh to properly capture the phase-field interface thickness (4 elements in the interface [95]) and the steepest gradients of $\widetilde{\zeta}_+$ and ϕ. We use a 120^3 tensor-product mesh with a mesh size of $0.4\,[\mu m]$ in the region of interest (bottom half of the domain). We partition the mesh into eight processors. Figure 7a identifies each core with a different color, showing that the tensor-product mesh can efficiently allocate resources in the region of interest (more resources/colors allocated to the bottom half of the domain). As in the previous 2D simulation, we apply a charging electro-potential value of $\phi_b = -0.7\,[V]$ to the cell, with an artificial nucleation region formed by a single protrusion (ellipsoidal seed), with its center at $(0; l_y/2; l_z/2)$, and semi-axes $4\,[\mu m] \times 2\,[\mu m] \times 2\,[\mu m]$ as Figure 7b shows. For visualization purpose, here we rotate the 3D figures to depict a vertical x-axis, showing an upright lithium dendrite growth, in agreement with the convention used for lithium dendrite experiments [83, 84, 94].

Figure 8 shows the morphological evolution of the simulated lithium dendrite (isosurface plot of the phase-field variable ξ). The simulation forms a spike-like, symmetric, and highly branched pattern, consisting of the main trunk and sets of four equal side branches growing in each horizontal direction. A result consistent with the body-centered cubic (bcc) crystallographic arrangement of lithium metal [67]. Our model includes the four folded surface anisotropy (6). In-situ optical microscopic investigations [83, 84] report spike-like lithium dendrite formation. These dendritic patterns grow when high (over-limiting) current densities are applied to the cell ($> 20\,\left[mA/cm^2\right]$) [6]. In such cases, the rate of lithium deposition overcomes the rate of solid-electrolyte interface formation, allowing the lithium deposit to grow almost free from the influence of the interface [6]. The enrichment of lithium-ion concentration appears in the vicinity of dendrite tips, reaching peak values of up to $\widetilde{\zeta}_+ = 2.1$, and triggering tip-growing dendritic lithium. Electrolyte regions with higher lithium-ion concentration ($\widetilde{\zeta}_+ > 1$) are represented by orange volumes in Figure 8. It is worth mentioning that this phenomenon was previously reported by Hong et al. [61] in 2D simulations of lithium dendrite formation, proposing a compositionally graded electrolyte, which could potentially suppress the dendrite initiation.

We calculate the electric field distribution by differentiation of the resolved electric potential $\vec{E} = -\nabla\phi$. The magnified view in Figure 9 shows how the electric field localizes in the vicinity of the dendrite tip, leading to an enriched concentration of the lithium-ion it induces due to the strong migration from the surrounding regions (see (9) and [61]).

Figure 10 shows the performance of the time-adaptive scheme, throughout the $0.6\,[s]$ of simulation. Starting with a small time-step of $\Delta t_0 = 10^{-7}\,[s]$ to achieve convergence, followed by a rapid increase in size, until reaching a stationary value of about $\Delta t_{n+1} = 10^{-3}\,[s]$. The evolution of the weighted truncation error e_{n+1} (blue) stays close to the minimum tolerance limit (10^{-7}) during $0.3\,[s]$ of simulation; beyond this point, the error estimate increases due to the acceleration of lithium dendrite propagation rate as the dendrites approach the positive electrode. The time-step size remains unchanged since the error estimate remains within the error bounds.

The construction of phase-field models satisfies an a priori nonlinear stability relationship, expressed as a time-decreasing free-energy functional; nevertheless, standard discrete approximations do not inherit this stability property. Thus, Figure 11 shows the evolution of the Gibbs free energy of the system Ψ, see (3), using our adaptive time integration scheme. We plot the total energy curve (black), as well as three additional energy curves that correspond to each one of its terms, namely, the Helmholtz (chemical) free energy $\int_V f_{ch}dV$ (blue), surface energy $\int_V f_{grad}dV$ (green), and electrostatic energy $\int_V f_{elec}dV$ (red), as the figure indicates. Figure 11 shows that the total systems' discrete free energy does not increase with time.

(A) $t = 0.1\,[s]$.   (B) $t = 0.2\,[s]$.   (C) $t = 0.3\,[s]$.

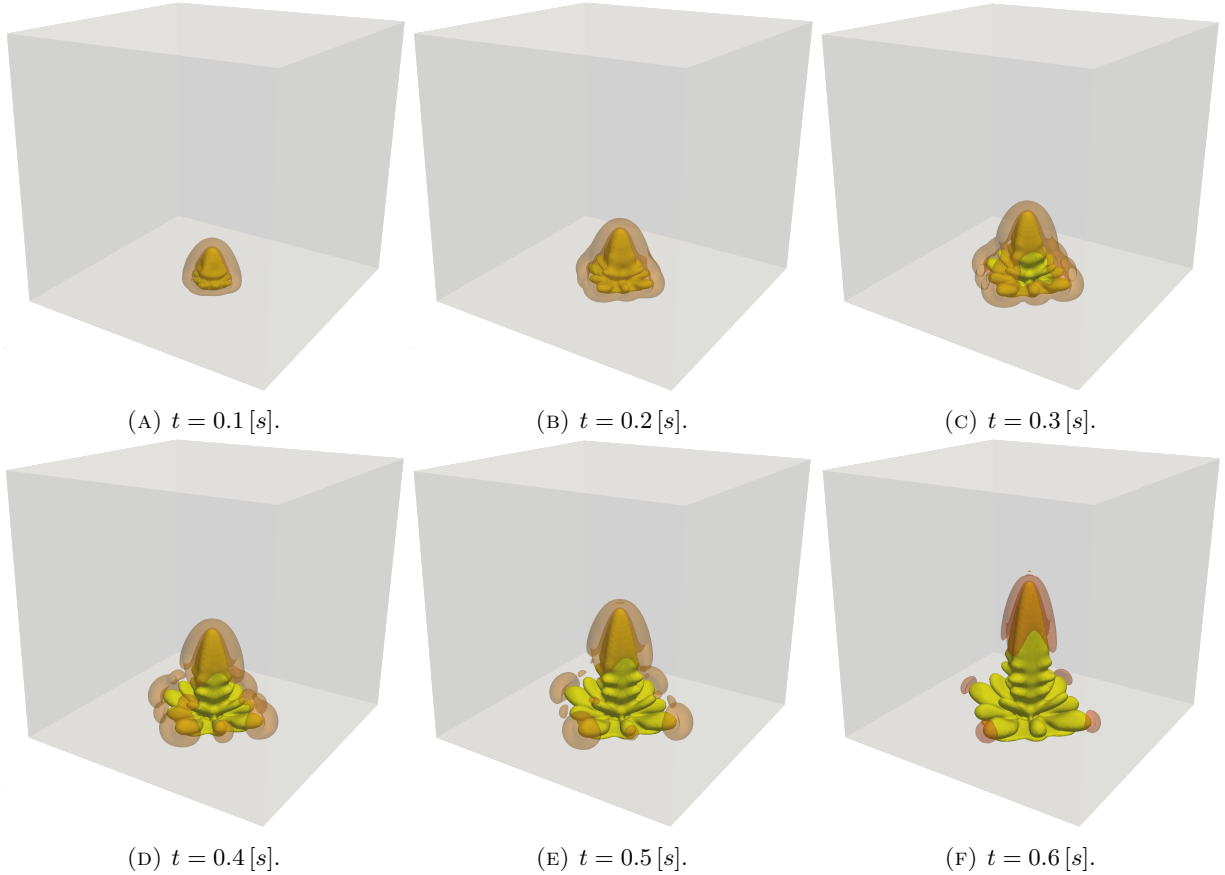(D) $t = 0.4\,[s]$.   (E) $t = 0.5\,[s]$.   (F) $t = 0.6\,[s]$.

FIGURE 8. Spike-like lithium dendrite formation under $\phi_b = -0.7\,[V]$ charging potential. The electrodeposited lithium is represented with a yellow isosurface plot of the phase-field variable ξ. Electrolyte regions with enriched concentration of lithium-ion ($\widetilde{\zeta}_+ > 1$) represented with orange volumes. Cube domain set as $80 \times 80 \times 80\,[\mu m^3]$.
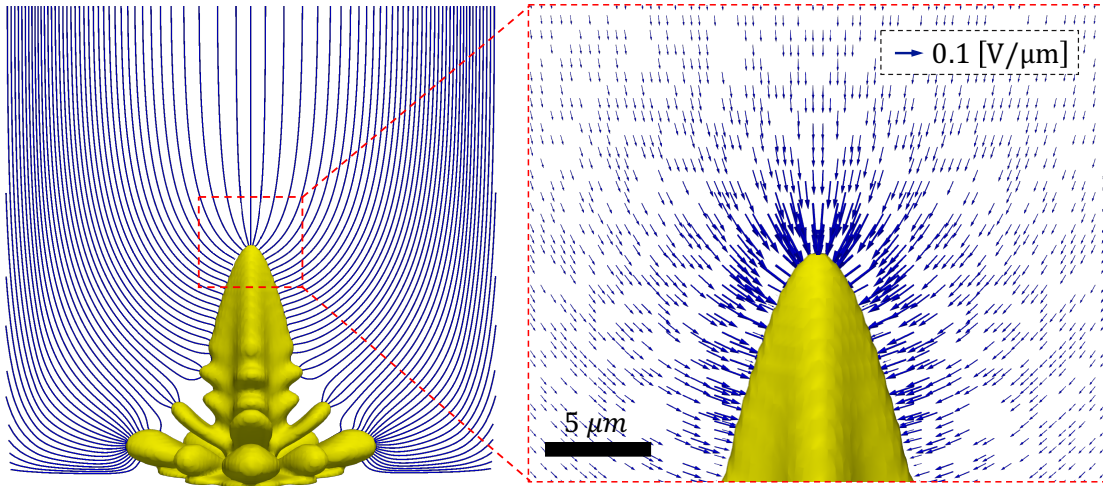
FIGURE 9. Overlay of electric field distribution (blue streamlines and vectors) with dendrite morphology at time $t = 0.5\,[s]$. Streamline plane set at $y = 40\,[\mu m]$.
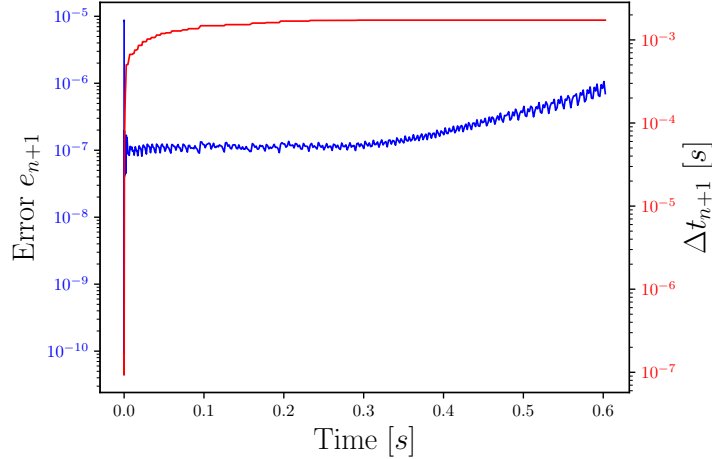
FIGURE 10. Time adaptivity for 3D spike-like dendrite growth simulation.
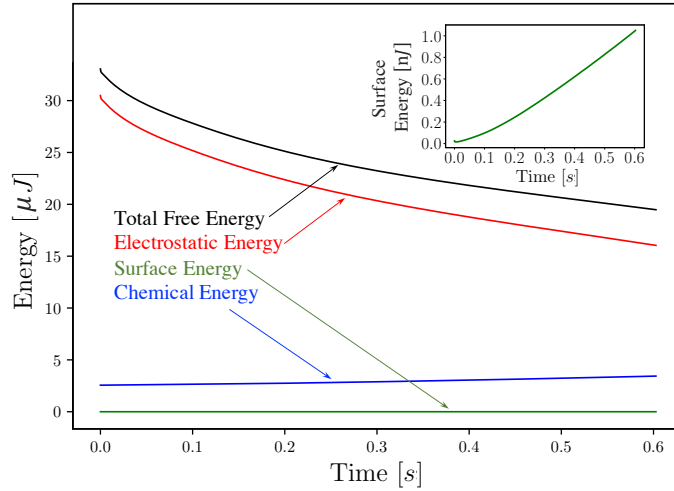
FIGURE 11. Energy time series for 3D spike-like dendrite growth simulation. The inset plots the increasing surface energy in smaller scale for better appreciation.

Therefore, we obtain discrete energy stable results using our second-order backward-difference (BDF2) time-adaptive marching scheme. Alternative, provably unconditionally stable second-order time accurate methods may deliver larger time-step sizes for phase-field models [110, 130–133], but these are beyond the scope of this work. Additionally, the system's chemical and surface energies increase as the lithium surface area grows as time progresses. In parallel, the electrostatic energy decreases in time. This interaction is consistent with the electrodeposition process, where the system stores the applied electrostatic energy as electrochemical energy as the battery charges.

6.5. **3D Simulation of lithium dendrite growth: Multi-nuclei experiment.** The lithium dendrite nucleation depends on local inhomogeneities that may arise from different causes, such as defects and impurities in the metal anode, imperfect contact between the electrode and electrolyte caused by the development of a solid-electrolyte interface, and variations in the local concentration or temperature in the electrolyte [66]. Given the random nature of the nucleation phenomenon, we need to deal with some degree of randomness and uncertainty when defining the artificial nuclei in the simulation. We study the simulations' sensitivity to the artificial nuclei size, shape, and proximity following 2D studies that show this dependance [62, 64, 67]. Thus, the following 3D numerical experiment tests the simulation's sensitivity to
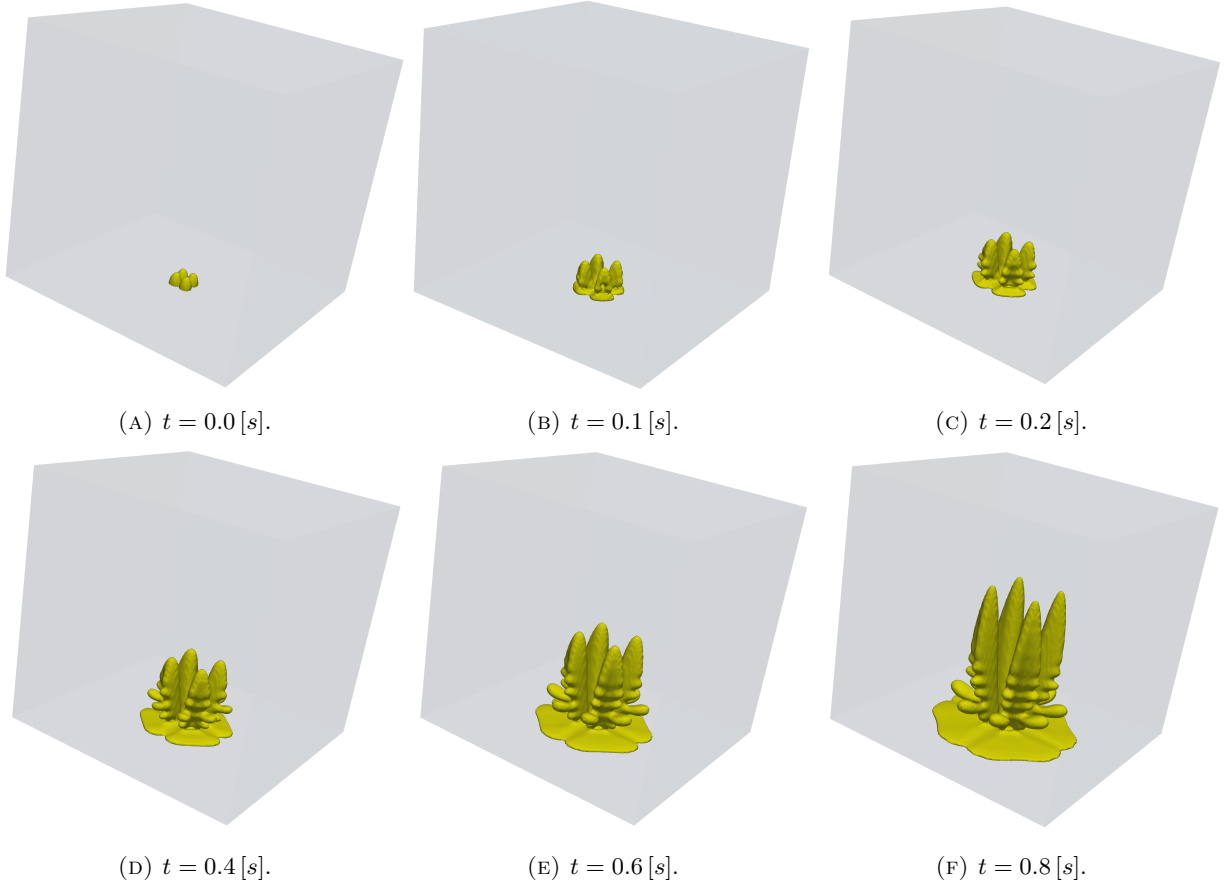
(A) $t = 0.0 \, [s]$.   (B) $t = 0.1 \, [s]$.   (C) $t = 0.2 \, [s]$.

(D) $t = 0.4 \, [s]$.   (E) $t = 0.6 \, [s]$.   (F) $t = 0.8 \, [s]$.

FIGURE 12. Spike-like lithium dendrite formation from multiple nucleation sites under $\phi_b = -0.7 \, [V]$ charging potential. The electrodeposited lithium is represented with a yellow isosurface plot of the phase-field variable ξ. Cube domain set as $80 \times 80 \times 80 \, [\mu m^3]$.

the nuclei distribution and proximity by comparing four-nuclei morphological results with those previously obtained with a single artificial protrusion. The simulation setup is similar to the previous 3D experiment with a different nucleation arrangement. Therefore, we form the artificial nucleation region with four protrusions (ellipsoidal seeds), with semi-axes $4 \, [\mu m] \times 2 \, [\mu m] \times 2 \, [\mu m]$, and centres located at $(y, x, z) = (0, 38, 38), (0, 42, 38), (0, 38, 42)$ and $(0, 42, 42)$.

Figure 12 shows the morphological evolution of the simulated lithium dendrite (isosurface plot of the phase-field variable ξ). In agreement with previous numerical experiments, the simulation forms a spike-like, symmetric, and highly branched pattern. The dendrite morphology consists of four main trunks growing from each nucleus, with pairs of orthogonal branches developing to the sides.

The dendrite growth does not occur perpendicular to the stack but at an angle of about $20°$ between main trunks. The stacks seem to repel each other, showing morphological similarity with dendritic patterns observed in lithium experiments performed by Ding [83] (see Figure 13a), and by Tatsuma [84] (see Figure 13b), under charging densities of $10 \, [mA/cm^2]$ and $3 \, [mA/cm^2]$, respectively. As a consequence of the reduced distance between electrodes (limited by the computational cost), the time scales we simulate are significantly shorter ($\sim$ two orders of magnitude faster) than the experimental ones [83, 84, 94].

Figure 14a details the simulated dendritic morphology at time $t = 0.5 \, [s]$, together with the spatial distribution of the lithium-ion concentration $\widetilde{\zeta}_+$ in the electrolyte region. No side branches form facing the center of the nucleation arrangement (between the dendrites), where the deposition process depletes the lithium-ion concentration (shown in blue). Figure 14a also shows how dendrite tips with higher lithium-ion concentration consume lithium ions from the dendrite valley [61], creating a shadow that inhibits branching growth in the spatial proximity of more developed adjacent dendrites. As a consequence, the side branches

(A) $10 \left[mA/cm^2 \right]$.

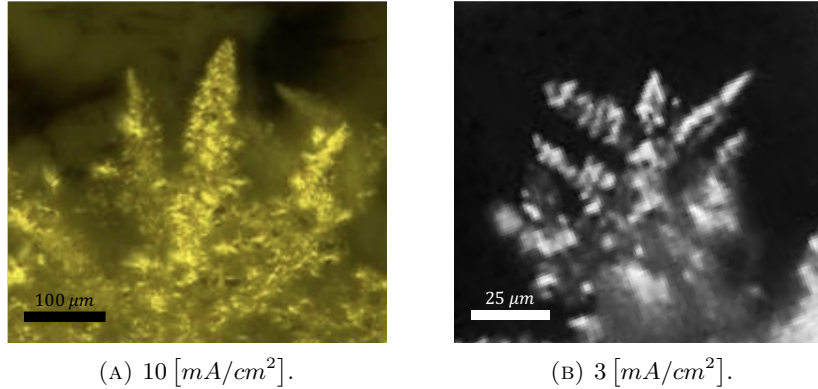(B) $3 \left[mA/cm^2 \right]$.

FIGURE 13. Photographs of lithium electrodes with electrochemical deposition of lithium. The deposition condition for (a), as performed by Ding [83], consist of $10 \left[mA/cm^2 \right]$ current density applied for 1 hour in 1M LiTFS/DME/DOL electrolyte, with working distance between electrodes set about $2 \left[mm \right]$. The deposition condition for (b), as performed by Tatsuma [84], consist of $3 \left[mA/cm^2 \right]$ current density applied for 1 hour in 1M LiClO$_4$ electrolyte, with working distance between electrodes set about $3 \left[mm \right]$.
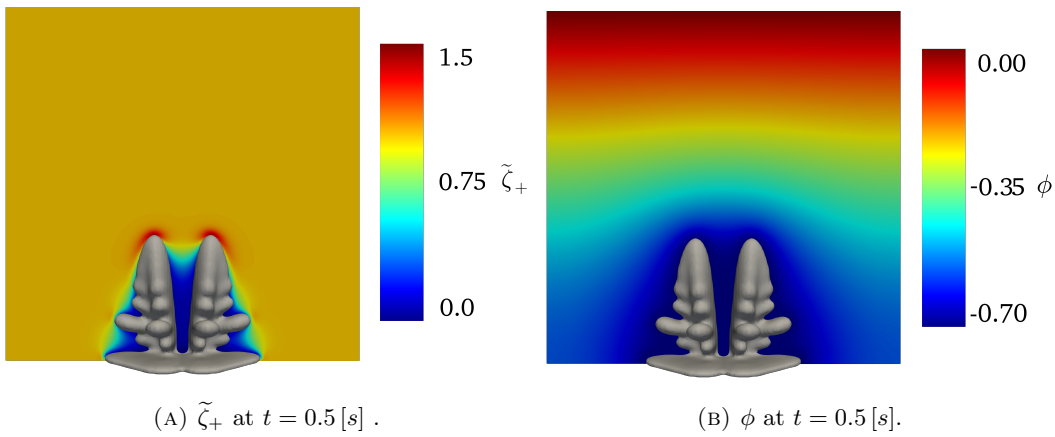
(A) $\widetilde{\zeta}_+$ at $t = 0.5 \left[s \right]$.

(B) ϕ at $t = 0.5 \left[s \right]$.

FIGURE 14. Spatial distribution overlay of lithium-ion concentration (a), and electric potential (b), with dendrite morphology at $t = 0.5 \left[s \right]$. Contour plane set at $y = 35 \left[\mu m \right]$.

do not grow dendrites facing the center of the nucleation arrangement (unfavorably oriented dendrites) due to the 3D interactions with other dendrites (adjacent to the main trunks) [100]. Therefore, 2D phase-field models of dendrite electrodeposition cannot capture this 3D phenomenon.

Figure 14b shows the spatial distribution of the electric potential ϕ overlaid with the lithium dendrite at the same instant $t = 0.5 \left[s \right]$. In agreement with the 2D simulations of Section 6.3, the electric potential has a steep gradient over the electrolyte phase and its steepness increases as the lithium dendrite grows.

Figure 15 shows the evolution of the electric field $\vec{E} = -\nabla \phi$ and the enriched lithium-ion concentration ($\widetilde{\zeta}_+ > 1$) in the vicinity of the dendrite tips (red volumes represent enriched concentration). As before, a larger electric field localizes in the vicinity of the dendrite tips, leading to a higher lithium-ion concentration with peak values of $\widetilde{\zeta}_+ = 1.8$. The electric migration forces overcome the concentration diffusion gradient and drive lithium cations from surrounding regions with lower concentrations (i.e., Li-ion depletion of valley regions) to accumulate around dendrite tips, triggering tip-growth with highly branched dendritic lithium.

We analyze the dendritic patterns' morphology evolution using single and multiple nuclei. Following Yufit et al. [128], we characterize the morphology by tracking the dendrites' volume-specific area ratio ($\mu m^2 / \mu m^3$) and the branch number evolution in time. Figure 16a plots the growth of the volume versus the surface area for the 3D lithium patterns we simulate. The volume-specific area average ratios of 0.83 and 0.91

(A) $t = 0.25\,[s]$.   (B) $t = 0.50\,[s]$.   (C) $t = 0.75\,[s]$.

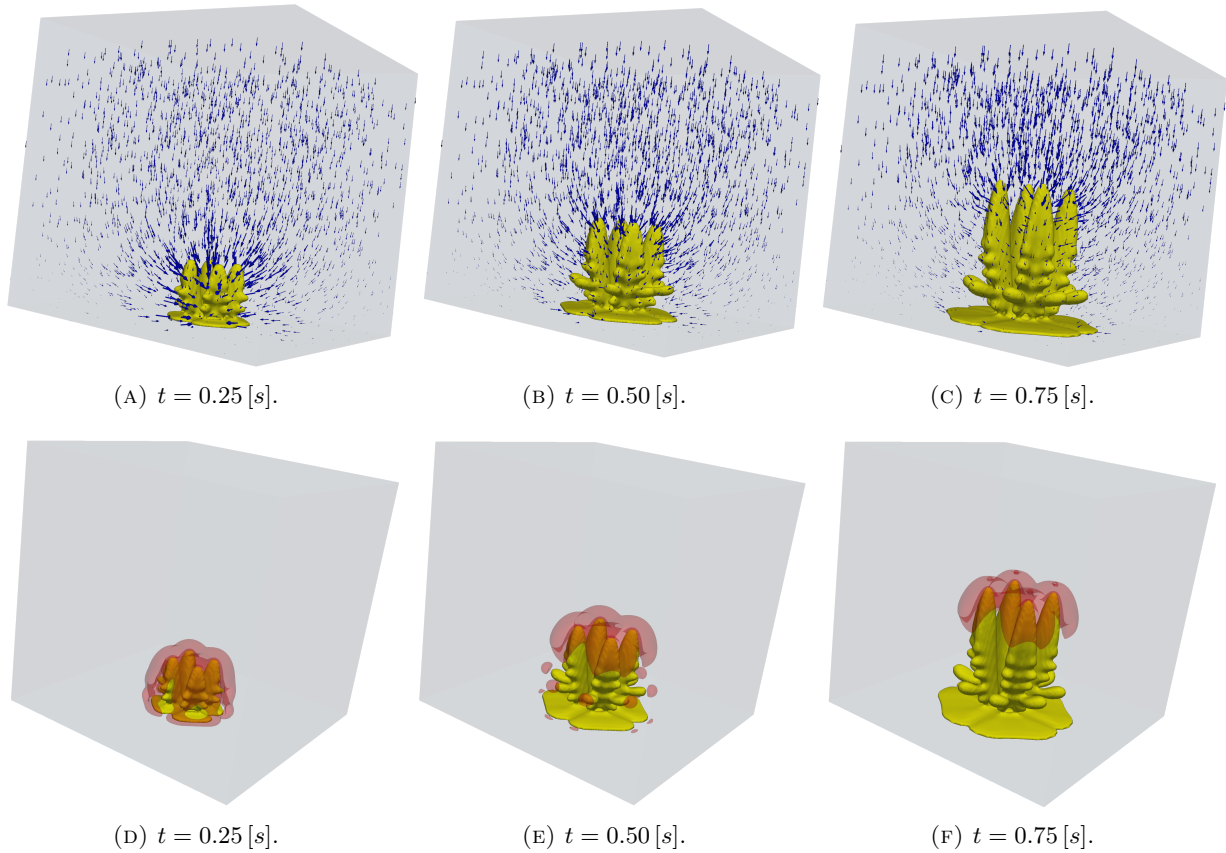(D) $t = 0.25\,[s]$.   (E) $t = 0.50\,[s]$.   (F) $t = 0.75\,[s]$.

FIGURE 15. Simulation of spike-like lithium dendrite formation from multiple nucleation sites. The upper row shows the overlay of the electric field evolution $\vec{E} = -\nabla\phi$ (blue vectors) with dendrite morphology; the second row exhibit the lithium ion enrichment effect $\widetilde{\zeta}_+ > 1$ (red volume) surrounding the dendrite tips.
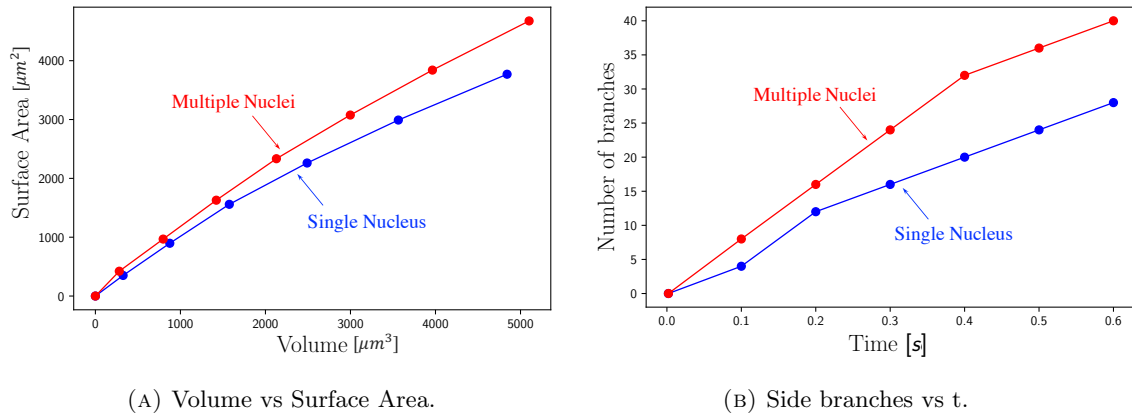

(A) Volume vs Surface Area.

(B) Side branches vs t.

FIGURE 16. Morphological comparison between 3D simulations of lithium dendrite growth (single and multiple-nuclei), in terms of the evolution of volume vs surface area ratio a, and number of side branches developed over time b.
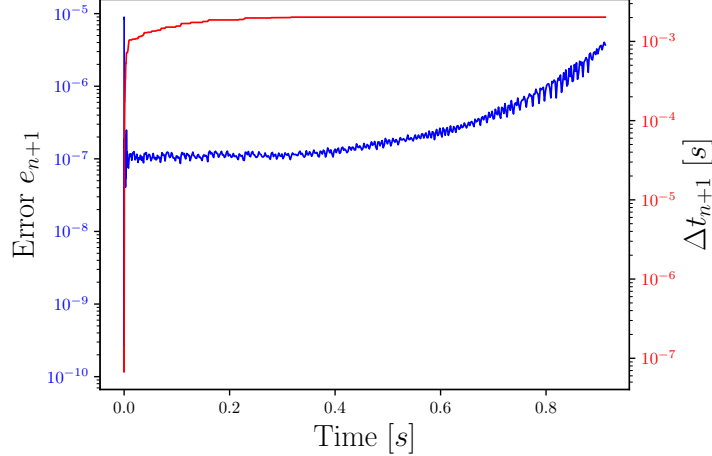
FIGURE 17. Time adaptivity plot for 3D spike-like four-nuclei dendrite growth simulation.

$\left[\mu m^2/\mu m^3\right]$ of the single and multiple nuclei simulations, respectively; where a higher surface area/volume ratio is indicative of a more branched shape. Given the lack of experimental data available in the literature for quantitative characterization of the spike-like lithium morphologies, we rely on experimental results available for zinc dendrites. Yufit et al. [128] report values between 0.86 and 1.04 $\left[\mu m^2/\mu m^3\right]$ for experimental formation of dendrites in zinc batteries. These values are slightly higher ratios than the ones we obtain for lithium. Nevertheless, these values are reasonable since zinc has a hexagonal crystal structure and tends to grow more branching (fractal) dendrites than lithium, which has a cubic crystal structure (less inherent anisotropy)and, thus, produces needle (spiky) dendrites [65]. Figure 16b compares the number of branches developed over time in each case. The simulatilons produce ratios of 48 and 72 branches per second $[1/[s]]$ for the single and multiple nuclei simulations, respectively. We compute the number of branches by visual inspection of the simulated morphologies, where we consider new protuberances as incipient branches under development. Direct comparison with dendrite experiments was impractical in this case, due to the faster dynamics of the simulation (small distance between electrodes).

Figure 17 shows the performance of the time-adaptive scheme, throughout the $0.8\,[s]$ of the simulation. Starting with a small time-step of $\Delta t_0 = 10^{-7}\,[s]$ to initially achieve convergence, followed by a rapid increase in size, until reaching a stationary value of about $\Delta t_{n+1} = 10^{-3}\,[s]$. The weighted truncation error e_{n+1} (blue) stays close to the minimum tolerance limit (10^{-7}) during $0.4\,[s]$ of the simulation, after which the estimated error grows due to the acceleration of lithium dendrite propagation rate as it approaches the positive electrode. The time-step size remains unchanged since the error estimate remains within the tolerances

Figure 18 shows the systems' energy evolution. The total energy curve (black) does not increase with time, showing energy stable results. As before, the system's chemical (blue) and surface energies (green) increase with time as the lithium surface area increases, while the electrostatic energy (red) decreases. This energy reduction happens as the process transforms electrostatic energy and stores it as electrochemical energy (battery charge). Figure 18 shows that the surface energy for the four-nuclei simulation is almost four times larger than the single nucleus surface energy of Figure 11. The proportionately larger surface area due to the four seeds explains this scaling.
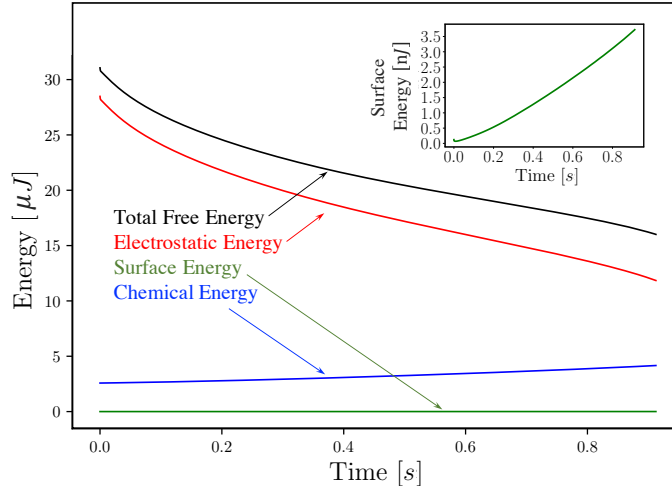
FIGURE 18. Energy time series for 3D spike-like four-nuclei dendrite growth simulation. The inset plots the increasing surface energy in smaller scale for better appreciation.

7. CONCLUSIONS

Using a phase-field model, we describe the dendrite formation process during metal (lithium) electrodeposition.   We present the weak variational form of the coupled equations describing electrochemical interactions during the battery charge cycle and its finite element implementation using an open-source library. We use a time-adaptive strategy and detail its implementation and parametrization. The numerical experiments demonstrate numerically that the adaptive strategy produces energy stable results when we use a minimum tolerance for the time-adaptive scheme of $\text{tol}_{\min} = 10^{-7}$. We reduce the computational cost of simulating the detailed lithium electrodeposition at the scale of the whole cell (distance between electrodes of about $l_x = 5000\,[\mu m]$) by using time-step size adaptivity, mesh mapping to concentrate the mesh in the region of interest, parallel computation, and a careful selection of the phase-field interface thickness (δ_{PF}) considering the applied electro potential value of $\phi_b = -0.45\,[V]$.

We compare our 2D simulation results (lithium dendrite propagation rate) with experimental measurements by Nishikawa et al. [94] at an applied current density of $i = 10\,[mA/cm^2]$. The growth rates we predict ($\sim 0.04\,[\mu m s^{-1}]$) are within the range of experimental results ($0.01 - 0.06\,[\mu m s^{-1}]$ [94]). Further, we compare the two-dimensional behavior of our model with previous phase-field simulations from the literature. The 2D evolution of the phase-field order parameter ξ under $\phi_b = -0.70\,[V]$ applied voltage depicts the dynamic growth of "bush-like" lithium dendrites. The spatial distribution of the lithium-ion concentration $\widetilde{\zeta}_+$, and electric potential ϕ, follow the same trend reported in [61, 67, 75].

We also perform 3D simulations of lithium dendrite formation to explain 3D highly branched "spike-like" dendritic patterns formed under high current density status (fast battery charge). We study the 3D morphological evolution of dendritic lithium under $\phi_b = -0.70\,[V]$ applied voltage. We mimic the cubic crystal structure and surface anisotropy of lithium by using a 3D four-fold anisotropy model (6) of William et al. [99] to simulate crystal growth.

We analyze the sensitivity of the model to initial conditions by comparing results using different setups (single nucleus versus a four-nuclei arrangement) for accounting for the random nature of the nucleation process. We obtain spike-like, symmetric, and highly-branched patterns in both cases. We obtain volume to specific-area average ratios of 0.83 and 0.91 $[\mu m^2/\mu m^3]$ for the single and multiple nuclei simulations, respectively; where a higher surface area/volume ratio indicates a more branched dendritic shape.

We study the 3D distribution of the electric field and lithium-ion concentration to better understand the mechanism behind spike-like dendrite growth. In both simulations, the electric field increases in the vicinity of the dendrite tips, increasing the lithium-ion concentration that peaks at $\widetilde{\zeta}_+ = 2.1$ for a single nucleus and 1.8 for multiple nuclei. Thus, electric migration forces overcome the concentration diffusion gradient, causing lithium cations to move from less concentrated surrounding regions (i.e., lithium-ion depletion of valley

regions) and accumulate around dendrite tips, triggering tip-growing and highly branched dendritic lithium. In multiple-nuclei simulation we observe that the deposition process depletes the lithium-ion concentration at the center of the nucleation arrangement. Thus, 3D interactions with other dendrites creates a shadow that inhibits branching growth in the spatial proximity of more developed adjacent dendrites [100]. Therefore, 2D phase-field models of dendrite electrodeposition cannot capture this 3D phenomenon.

The analysis reveals that dendrite formation is connected to the competition between the lithium cation diffusion and electric migration forces, generating an uneven distribution of Li^+ on the electrode surface. This fact gives insight into strategies of dendrite suppression. For example, the use of pulse charging in lithium batteries can shift the competition in favour of cation diffusion (concentration gradient), by allowing resting times (milliseconds) for lithium cations to diffuse from dendrites' tips to less concentrated surrounding regions (valleys), leading to dendrite inhibition [18, 19, 74]. Furthermore, other strategies such as the application of electrolyte flow, increment of the internal temperature, or improvements in the electrolyte composition, can enhance the diffusion of lithium ions with the purpose of achieving a more uniform concentration field on the anode surface, leading to lower dendrite formation propensity [22–35].

Finally, unlike 2D simulations, the 3D simulations performed have a smaller domain size due to the high computational cost. Consequently, the short separation between electrodes in the 3D model ($l_x = 80\,[\mu m]$) induces faster deposition rates. Thus, future work may explore different meshing strategies to simulate larger 3D domains to achieve realistic simulation time scales.

In conclusion, we demonstrate the proposed phase-field modeling framework's effectiveness in performing 2D and 3D simulations of dendrite formation in lithium metal batteries with a reasonable computational cost. Beyond lithium electrodeposition, the framework has the potential to model other metal deposits in metal-anode batteries, such as zinc anode batteries.

8. Acknowledgments

References

[1] Wu Xu, Jiulin Wang, Fei Ding, Xilin Chen, Eduard Nasybulin, Yaohui Zhang, and Ji-Guang Zhang. Lithium metal anodes for rechargeable batteries. *Energy Environ. Sci.*, 7:513–537, 2014.

[2] Jing Fu, Zachary Paul Cano, Moon Gyu Park, Aiping Yu, Michael Fowler, and Zhongwei Chen. Electrically rechargeable zinc–air batteries: Progress, challenges, and perspectives. *Advanced Materials*, 29(7):1604685, 2017.

[3] Yanguang Li and Jun Lu. Metal–air batteries: Will they be the future electrochemical energy storage device of choice? *ACS Energy Letters*, 2(6):1370–1377, 2017.

[4] Zhe Li, Jun Huang, Bor Yann Liaw, Viktor Metzler, and Jianbo Zhang. A review of lithium deposition in lithium-ion and lithium metal secondary batteries. *Journal of power sources*, 254:168–182, 2014.

[5] Bin Liu, Ji-Guang Zhang, and Wu Xu. Advancing lithium metal batteries. *Joule*, 2(5):833–845, 2018.

[6] Peng Bai, Jinzhao Guo, Miao Wang, Akihiro Kushima, Liang Su, Ju Li, Fikile R. Brushett, and Martin Z. Bazant. Interactions between lithium growths and nanoporous ceramic separators. *Joule*, 2(11):2434–2449, 2018.

[7] Peter G Bruce, Stefan A Freunberger, Laurence J Hardwick, and Jean-Marie Tarascon. Li–O$_2$ and Li–S batteries with high energy storage. *Nature materials*, 11(1):19–29, 2012.

[8] Brian D. Adams, Jianming Zheng, Xiaodi Ren, Wu Xu, and Ji-Guang Zhang. Accurate determination of coulombic efficiency for lithium metal anodes and lithium metal batteries. *Advanced Energy Materials*, 8(7):1702097, 2018.

[9] Michel Rosso, Claire Brissot, Anna Teyssot, Mickaël Dollé, Lucas Sannier, Jean-Marie Tarascon, Renaud Bouchet, and Stéphane Lascaud. Dendrite short-circuit and fuse effect on Li/polymer/Li cells. *Electrochimica Acta*, 51(25):5334–5340, 2006.

[10] Dongping Lu, Yuyan Shao, Terence Lozano, Wendy D. Bennett, Gordon L. Graff, Bryant Polzin, Jiguang Zhang, Mark H. Engelhard, Natalio T. Saenz, Wesley A. Henderson, Priyanka Bhattacharya, Jun Liu, and Jie Xiao. Failure mechanism for fast-charged lithium metal batteries with liquid electrolytes. *Advanced Energy Materials*, 5(3):1400993, 2015.

[11] Shuhong Jiao, Jianming Zheng, Qiuyan Li, Xing Li, Mark H. Engelhard, Ruiguo Cao, Ji-Guang Zhang, and Wu Xu. Behavior of lithium metal anodes under various capacity utilization and high current density in lithium metal batteries. *Joule*, 2(1):110–124, 2018.

[12] Lei Fan, Houlong L. Zhuang, Weidong Zhang, Yao Fu, Zhihao Liao, and Yingying Lu. Stable lithium electrodeposition at ultra-high current densities enabled by 3D PMF/Li composite anode. *Advanced Energy Materials*, 8(15):1703360, 2018.

[13] Nan Li, Qian Ye, Kun Zhang, Huibo Yan, Chao Shen, Bingqing Wei, and Keyu Xie. Normalized lithium growth from the nucleation stage for dendrite-free lithium metal anodes. *Angewandte Chemie International Edition*, 58(50):18246–18251, 2019.

[14] Chanyuan Zhang, Shan Liu, Guojie Li, Cuijuan Zhang, Xingjiang Liu, and Jiayan Luo. Incorporating ionic paths into 3D conducting scaffolds for high volumetric and areal capacity, high rate lithium-metal anodes. *Advanced Materials*, 30(33):1801328, 2018.

[15] Wenwu Zhong, Zongpeng Wang, Nan Gao, Liangai Huang, Zhiping Lin, Yanping Liu, Fanqi Meng, Jun Deng, Shifeng Jin, Qinghua Zhang, et al. Coupled vacancy pairs in Ni-doped CoSe for improved electrocatalytic hydrogen production through topochemical deintercalation. *Angewandte Chemie*, 132(50):22931–22936, 2020.

[16] Shijie Shen, Zongpeng Wang, Zhiping Lin, Kai Song, Qinghua Zhang, Fanqi Meng, Lin Gu, and Wenwu Zhong. Crystalline-amorphous interfaces coupling of $CoSe_2$/CoP with optimized d-band center and boosted electrocatalytic hydrogen evolution. *Advanced Materials*, page 2110631, 2022.

[17] Zongpeng Wang, Shijie Shen, Zhiping Lin, Weiying Tao, Qinghua Zhang, Fanqi Meng, Lin Gu, and Wenwu Zhong. Regulating the local spin state and band structure in Ni_3S_2 nanosheet for improved oxygen evolution activity. *Advanced Functional Materials*, page 2112832, 2022.

[18] Heng Yang, Edmond O. Fey, Bryan D. Trimm, Nikolay Dimitrov, and M. Stanley Whittingham. Effects of pulse plating on lithium electrodeposition, morphology and cycling efficiency. *Journal of Power Sources*, 272:900–908, 2014.

[19] Matthew Z. Mayers, Jakub W. Kaminski, and Thomas F. Miller. Suppression of dendrite formation via pulse charging in rechargeable lithium metal batteries. *The Journal of Physical Chemistry C*, 116(50):26214–26221, 2012.

[20] Asghar Aryanfar, Daniel Brooks, Boris V. Merinov, William A. Goddard, Agustín J. Colussi, and Michael R. Hoffmann. Dynamics of lithium dendrite growth and inhibition: Pulse charging experiments and monte carlo calculations. *The Journal of Physical Chemistry Letters*, 5(10):1721–1726, 2014.

[21] Mukul D. Tikekar, Lynden A. Archer, and Donald L. Koch. Stability analysis of electrodeposition across a structured electrolyte with immobilized anions. *Journal of The Electrochemical Society*, 161(6):A847–A855, 2014.

[22] Lars-Göran Sundström and Fritz H. Bark. On morphological instability during electrodeposition with a stagnant binary electrolyte. *Electrochimica Acta*, 40(5):599–614, 1995.

[23] Guoxing Li, Yue Gao, Xin He, Qingquan Huang, Shuru Chen, Seong H. Kim, and Donghai Wang. Organosulfide-plasticized solid-electrolyte interphase layer enables stable lithium metal anodes for long-cycle lithium-sulfur batteries. *Nature Communications*, 8(1):850, Oct 2017.

[24] Jianming Zheng, Mark H. Engelhard, Donghai Mei, Shuhong Jiao, Bryant J. Polzin, Ji-Guang Zhang, and Wu Xu. Electrolyte additive enabled fast charging and stable cycling lithium metal batteries. *Nature Energy*, 2(3):17012, Mar 2017.

[25] Jiangfeng Qian, Wesley A. Henderson, Wu Xu, Priyanka Bhattacharya, Mark Engelhard, Oleg Borodin, and Ji-Guang Zhang. High rate and stable cycling of lithium metal anode. *Nature Communications*, 6(1):6362, Feb 2015.

[26] Liumin Suo, Yong-Sheng Hu, Hong Li, Michel Armand, and Liquan Chen. A new class of solvent-in-salt electrolyte for high-energy rechargeable metallic lithium batteries. *Nature Communications*, 4(1):1481, Feb 2013.

[27] Patrick J. Kim, Kyungho Kim, and Vilas G. Pol. Uniform metal-ion flux through interface-modified membrane for highly stable metal batteries. *Electrochimica Acta*, 283:517–527, 2018.

[28] Xin-Bing Cheng, Ting-Zheng Hou, Rui Zhang, Hong-Jie Peng, Chen-Zi Zhao, Jia-Qi Huang, and Qiang Zhang. Dendrite-free lithium deposition induced by uniformly distributed lithium ions for efficient lithium metal batteries. *Advanced Materials*, 28(15):2888–2895, 2016.

[29] Xuelin Yang, Zhaoyin Wen, Xiujian Zhu, and Shahua Huang. Electrodeposition of lithium film under dynamic conditions and its application in all-solid-state rechargeable lithium battery. *Solid State Ionics*, 176(11-12):1051–1055, 2005.

[30] Aoxuan Wang, Qibo Deng, Lijun Deng, Xuze Guan, and Jiayan Luo. Eliminating tip dendrite growth by lorentz force for stable lithium metal anodes. *Advanced Functional Materials*, 29(25):1902630, 2019.

[31] Jinwang Tan and Emily M. Ryan. Computational study of electro-convection effects on dendrite growth in batteries. *Journal of Power Sources*, 323:67–77, 2016.

[32] Owen Crowther and Alan C. West. Effect of electrolyte composition on lithium dendrite growth. *Journal of The Electrochemical Society*, 155(11):A806, 2008.

[33] A. Wlasenko, F. Soltani, D. Zakopcan, D. Sinton, and G. M. Steeves. Diffusion-limited and advection-driven electrodeposition in a microfluidic channel. *Phys. Rev. E*, 81:021601, Feb 2010.

[34] Guoxing Li, Zhe Liu, Qingquan Huang, Yue Gao, Michael Regula, Daiwei Wang, Long-Qing Chen, and Donghai Wang. Stable metal battery anodes enabled by polyethylenimine sponge hosts by way of electrokinetic effects. *Nature Energy*, 3(12):1076–1083, Dec 2018.

[35] Brian D. Iverson and Suresh V. Garimella. Recent advances in microscale pumping technologies: A review and evaluation. *Microfluidics and Nanofluidics*, 5(2):145–174, Aug 2008.

[36] L. Gireaud, S. Grugeon, S. Laruelle, B. Yrieix, and J.-M. Tarascon. Lithium metal stripping/plating mechanisms studies: A metallurgical approach. *Electrochemistry Communications*, 8(10):1639–1649, 2006.

[37] Rohan Akolkar. Modeling dendrite growth during lithium electrodeposition at sub-ambient temperature. *Journal of Power Sources*, 246:84–89, 2014.

[38] H.H. Yan, Y.H. Bie, X.Y. Cui, G.P. Xiong, and L. Chen. A computational investigation of thermal effect on lithium dendrite growth. *Energy Conversion and Management*, 161:193–204, 2018.

[39] Yayuan Liu, Dingchang Lin, Pak Yan Yuen, Kai Liu, Jin Xie, Reinhold H. Dauskardt, and Yi Cui. An artificial solid electrolyte interphase with high Li-ion conductivity, mechanical strength, and flexibility for stable lithium metal anodes. *Advanced Materials*, 29(10):1605531, 2017.

[40] Bin Zhu, Yan Jin, Xiaozhen Hu, Qinghui Zheng, Su Zhang, Qianjin Wang, and Jia Zhu. Poly(dimethylsiloxane) thin film as a stable interfacial layer for high-performance lithium-metal battery anodes. *Advanced Materials*, 29(2):1603755, 2017.

[41] Qiang Zhao, Xin Chen, Wang Hou, Beirong Ye, Yongqi Zhang, Xinhui Xia, and Jinshu Wang. A facile, scalable, high stability lithium metal anode. *SusMat*, 2022.

[42] Peng Bai, Ju Li, Fikile R. Brushett, and Martin Z. Bazant. Transition of lithium growth mechanisms in liquid electrolytes. *Energy Environ. Sci.*, 9:3221–3229, 2016.

[43] He Liu, Xin-Bing Cheng, Zhehui Jin, Rui Zhang, Guoxiu Wang, Long-Qing Chen, Quan-Bing Liu, Jia-Qi Huang, and Qiang Zhang. Recent advances in understanding dendrite growth on alkali metal anodes. *EnergyChem*, 1(1):100003, 2019.

[44] Xin-Bing Cheng, Rui Zhang, Chen-Zi Zhao, and Qiang Zhang. Toward safe lithium metal anode in rechargeable batteries: A review. *Chemical reviews*, 117(15):10403–10473, 2017.

[45] Aniruddha Jana and R. Edwin García. Lithium dendrite growth mechanisms in liquid electrolytes. *Nano Energy*, 41:552–565, 2017.

[46] Peng Tan, Wei Kong, Zongping Shao, Meilin Liu, and Meng Ni. Advances in modeling and simulation of Li–air batteries. *Progress in Energy and Combustion Science*, 62:155–189, 2017.

[47] Markus Jäckle and Axel Groß. Microscopic properties of lithium, sodium, and magnesium battery anode materials related to possible dendrite growth. *The Journal of Chemical Physics*, 141(17):174710, 2014.

[48] Chen Ling, Debasish Banerjee, and Masaki Matsui. Study of the electrochemical deposition of Mg in the atomic level: Why it prefers the non-dendritic morphology. *Electrochimica Acta*, 76:270–274, 2012.

[49] Yalcin Ozhabes, Deniz Gunceler, and T. A. Arias. Stability and surface diffusion at lithium-electrolyte interphases with connections to dendrite suppression, 2015.

[50] J.-N. Chazalviel. Electrochemical aspects of the generation of ramified metallic electrodeposits. *Phys. Rev. A*, 42:7355–7367, Dec 1990.

[51] J. L. Barton, J. Oapos;m. Bockris, and Alfred Rene Jean Paul Ubbelohde. The electrolytic growth of dendrites from ionic solutions. *Proceedings of the Royal Society of London. Series A. Mathematical and Physical Sciences*, 268(1335):485–505, 1962.

[52] Charles Monroe and John Newman. The effect of interfacial deformation on electrodeposition kinetics. *Journal of The Electrochemical Society*, 151(6):A880, 2004.

[53] Dong Wang, Wei Zhang, Weitao Zheng, Xiaoqiang Cui, Teófilo Rojo, and Qiang Zhang. Towards high-safe lithium metal anodes: Suppressing lithium dendrites via tuning surface energy. *Advanced science (Weinheim, Baden-Wurttemberg, Germany)*, 4(1):1600168–1600168, 2016.

[54] Kai Jiang, Xunliang Liu, Xiaoping Yi, Guofeng Lou, Zhi Wen, and Lin Liu. Modeling of solid-state lithium-oxygen battery with porous $Li_{1.3}Al_{0.3}Ti_{1.7}(PO_4)_3$-based cathode. *Journal of Energy Storage*, 45:103747, 2022.

[55] J. E. Guyer, W. J. Boettinger, J. A. Warren, and G. B. McFadden. Phase field modeling of electrochemistry. I. Equilibrium. *Phys. Rev. E*, 69:021603, 2004.

[56] J. E. Guyer, W. J. Boettinger, J. A. Warren, and G. B. McFadden. Phase field modeling of electrochemistry. II. Kinetics. *Phys. Rev. E*, 69:021604, Feb 2004.

[57] Yasushi Shibuta, Yoshinao Okajima, and Toshio Suzuki. Phase-field modeling for electrodeposition process. *Science and Technology of Advanced Materials*, 8(6):511–518, 2007. Nanoionics - Present and future prospects.

[58] Yoshinao Okajima, Yasushi Shibuta, and Toshio Suzuki. A phase-field model for electrode reactions with Butler–Volmer kinetics. *Computational Materials Science*, 50(1):118–124, 2010.

[59] Linyun Liang, Yue Qi, Fei Xue, Saswata Bhattacharya, Stephen J. Harris, and Long-Qing Chen. Nonlinear phase-field model for electrode-electrolyte interface evolution. *Phys. Rev. E*, 86:051609, 2012.

[60] Martin Z. Bazant. Theory of chemical kinetics and charge transfer based on nonequilibrium thermodynamics. *Accounts of Chemical Research*, 46(5):1144–1160, 2013.

[61] Linyun Liang and Long-Qing Chen. Nonlinear phase field model for electrodeposition in electrochemical systems. *Applied Physics Letters*, 105(26):263903, 2014.

[62] David R. Ely, Aniruddha Jana, and R. Edwin García. Phase field kinetics of lithium electrodeposits. *Journal of Power Sources*, 272:581–594, 2014.

[63] H.-W. Zhang, Z. Liu, L. Liang, L. Chen, Y. Qi, S. J. Harris, P. Lu, and L.-Q. Chen. Understanding and predicting the lithium dendrite formation in Li-ion batteries: Phase field model. *ECS Transactions*, 61(8):1–9, sep 2014.

[64] Lei Chen, Hao Wei Zhang, Lin Yun Liang, Zhe Liu, Yue Qi, Peng Lu, James Chen, and Long-Qing Chen. Modulation of dendritic patterns during electrodeposition: A nonlinear phase-field model. *Journal of Power Sources*, 300:376–385, 2015.

[65] Daniel A. Cogswell. Quantitative phase-field modeling of dendritic electrodeposition. *Phys. Rev. E*, 92:011301, 2015.

[66] Zijian Hong and Venkatasubramanian Viswanathan. Phase-field simulations of lithium dendrite growth with open-source software. *ACS Energy Letters*, 3(7):1737–1743, 2018.

[67] Vitaliy Yurkiv, Tara Foroozan, Ajaykrishna Ramasubramanian, Reza Shahbazian-Yassar, and Farzad Mashayek. Phase-field modeling of solid electrolyte interface (SEI) influence on Li dendritic behavior. *Electrochimica Acta*, 265:609–619, 2018.

[68] Wenyu Mu, Xunliang Liu, Zhi Wen, and Lin Liu. Numerical simulation of the factors affecting the growth of lithium dendrites. *Journal of Energy Storage*, 26:100921, 2019.

[69] Aniruddha Jana, Sang Inn Woo, KSN Vikrant, and R Edwin García. Electrochemomechanics of lithium dendrite growth. *Energy & Environmental Science*, 12(12):3595–3607, 2019.

[70] Yangyang Liu, Xieyu Xu, Matthew Sadd, Olesya O. Kapitanova, Victor A. Krivchenko, Jun Ban, Jialin Wang, Xingxing Jiao, Zhongxiao Song, Jiangxuan Song, Shizhao Xiong, and Aleksandar Matic. Insight into the critical role of exchange current density on electrodeposition behavior of lithium metal. *Advanced Science*, 8(5):2003301, 2021.

[71] Pengjian Guan, Lin Liu, and Xianke Lin. Simulation and experiment on solid electrolyte interphase (SEI) morphology evolution and lithium-ion diffusion. *Journal of The Electrochemical Society*, 162(9):A1798, 2015.

[72] Pengjian Guan, Lin Liu, and Yang Gao. Phase-field modeling of solid electrolyte interphase (SEI) cracking in lithium batteries. *ECS Transactions*, 85(13):1041, 2018.

[73] Lin Liu and Pengjian Guan. Phase-field modeling of solid electrolyte interphase (SEI) evolution: Considering cracking and dissolution during battery cycling. *ECS Transactions*, 89(1):101, 2019.

[74] Dongge Qiao, Xunliang Liu, Ruifeng Dou, Zhi Wen, Wenning Zhou, and Lin Liu. Quantitative analysis of the inhibition effect of rising temperature and pulse charging on lithium dendrite growth. *Journal of Energy Storage*, 49:104137, 2022.

[75] Chih-Hung Chen and Chun-Wei Pao. Phase-field study of dendritic morphology in lithium metal batteries. *Journal of Power Sources*, 484:229203, 2021.

[76] Jiawei Zhang, Yuanpeng Liu, Changguo Wang, and Huifeng Tan. An electrochemical-mechanical phase field model for lithium dendrite. *Journal of The Electrochemical Society*, 168(9):090522, 2021.

[77] Sybren Ruurds de Groot and Peter Mazur. *Non-equilibrium Thermodynamics*. Courier Corporation, 1984.

[78] I. Steinbach, F. Pezzolla, B. Nestler, M. Seeßelberg, R. Prieler, G.J. Schmitz, and J.L.L. Rezende. A phase field concept for multiphase systems. *Physica D: Nonlinear Phenomena*, 94(3):135–147, 1996.

[79] R.Edwin García, Catherine M Bishop, and W.Craig Carter. Thermodynamically consistent variational principles with applications to electrically and magnetically active systems. *Acta Materialia*, 52(1):11–21, 2004.

[80] B.C. Han, A. Van der Ven, D. Morgan, and G. Ceder. Electrochemical modeling of intercalation processes with phase field models. *Electrochimica Acta*, 49(26):4691–4699, 2004.

[81] S.M Allen and J.W Cahn. Ground state structures in ordered binary alloys with second neighbor interactions. *Acta Metallurgica*, 20(3):423–433, 1972.

[82] Qiao Wang, Geng Zhang, Yajie Li, Zijian Hong, Da Wang, and Siqi Shi. Application of phase-field method in rechargeable batteries. *npj Computational Materials*, 6(1):1–8, 2020.

[83] Tianyao Ding. In-situ optical microscopic investigation of the dendrite formation on lithium anode under different electrolyte conditions in Li-S battery. 2016.

[84] Tetsu Tatsuma, Makoto Taguchi, and Noboru Oyama. Inhibition effect of covalently cross-linked gel electrolytes on lithium dendrite formation. *Electrochimica Acta*, 46(8):1201–1205, 2001.

[85] Chun-Peng Yang, Ya-Xia Yin, Shuai-Feng Zhang, Nian-Wu Li, and Yu-Guo Guo. Accommodating lithium into 3D current collectors with a submicron skeleton towards long-life lithium metal anodes. *Nature communications*, 6(1):1–9, 2015.

[86] Yongling An, Huifang Fei, Guifang Zeng, Xiaoyan Xu, Lijie Ci, Baojuan Xi, Shenglin Xiong, Jinkui Feng, and Yitai Qian. Vacuum distillation derived 3D porous current collector for stable lithium–metal batteries. *Nano Energy*, 47:503–511, 2018.

[87] Yuan Tian, Yongling An, Chuanliang Wei, Baojuan Xi, Shenglin Xiong, Jinkui Feng, and Yitai Qian. Flexible and free-standing $Ti_3C_2T_x$ MXeneZn paper for dendrite-free aqueous zinc metal batteries and nonaqueous lithium metal batteries. *ACS nano*, 13(10):11676–11685, 2019.

[88] Linghong Xu, Zhihao Yu, and Junrong Zheng. Dendrite-free lithium electrodeposition enabled by 3D porous lithiophilic host toward stable lithium metal anodes. *Oxford Open Materials Science*, 1(1):itab013, 2021.

[89] PP Natsiavas, K Weinberg, D Rosato, and M Ortiz. Effect of prestress on the stability of electrode–electrolyte interfaces during charging in lithium batteries. *Journal of the Mechanics and Physics of Solids*, 95:92–111, 2016.

[90] Inhyuk Jang and Arun Yethiraj. Effect of diffusion constant on the morphology of dendrite growth in lithium metal batteries. *The Journal of Chemical Physics*, 154(23):234705, 2021.

[91] Klaus J. Vetter, editor. *Electrochemical Kinetics*. Academic Press, 1967.

[92] Allen J. Bard and Larry R. Faulkner, editors. *Electrochemical Methods: Fundamentals and Applications*. Wiley, 2001.

[93] Alexander M. Kuznetsov and Jens Ulstrup. *Electron Transfer in Chemistry and Biology: An Introduction to the Theory*. Wiley, 1999.

[94] Kei Nishikawa, Takeshi Mori, Tetsuo Nishida, Yasuhiro Fukunaka, and Michel Rosso. Li dendrite growth and Li^+ ionic mass transfer phenomenon. *Journal of Electroanalytical Chemistry*, 661(1):84–89, 2011.

[95] Marcos Exequiel Arguello, Monica Gumulya, Jos Derksen, Ranjeet Utikar, and Victor Manuel Calo. Phase-field modeling of planar interface electrodeposition in lithium-metal batteries. *Journal of Energy Storage*, 50:104627, 2022.

[96] Ryo Kobayashi. Modeling and numerical simulations of dendritic crystal growth. *Physica D: Nonlinear Phenomena*, 63(3):410–423, 1993.

[97] Richard Tran, Xiang-Guo Li, Joseph H. Montoya, Donald Winston, Kristin Aslaug Persson, and Shyue Ping Ong. Anisotropic work function of elemental crystals. *Surface Science*, 687:48–55, 2019.

[98] Hui Zheng, Xiang-Guo Li, Richard Tran, Chi Chen, Matthew Horton, Donald Winston, Kristin Aslaug Persson, and Shyue Ping Ong. Grain boundary properties of elemental metals. *Acta Materialia*, 186:40–49, 2020.

[99] William L. George and James A. Warren. A parallel 3D dendritic growth simulator using the phase-field method. *Journal of Computational Physics*, 177(2):264–283, 2002.

[100] Tomohiro Takaki, Takashi Shimokawabe, Munekazu Ohno, Akinori Yamanaka, and Takayuki Aoki. Unexpected selection of growing dendrites by very-large-scale phase-field simulation. *Journal of Crystal Growth*, 382:21–25, 2013.

[101] K. R. Elder, Martin Grant, Nikolas Provatas, and J. M. Kosterlitz. Sharp interface limits of phase-field models. *Phys. Rev. E*, 64:021604, Jul 2001.

[102] John W. Cahn and John E. Hilliard. Free energy of a nonuniform system. III. Nucleation in a two-component incompressible fluid. *The Journal of Chemical Physics*, 31(3):688–699, 1959.

[103] Min Chai, Kun Luo, Changxiao Shao, and Jianren Fan. An efficient level set remedy approach for simulations of two-phase flow based on sigmoid function. *Chemical Engineering Science*, 172:335–352, 2017.

[104] W. J. Boettinger, J. A. Warren, C. Beckermann, and A. Karma. Phase-field simulation of solidification. *Annual Review of Materials Research*, 32(1):163–194, 2002.

[105] Juan Elezgaray, Christophe Léger, and Françoise Argoul. Linear stability analysis of unsteady galvanostatic electrodeposition in the two-dimensional diffusion-limited regime. *Journal of The Electrochemical Society*, 145:2016–2024, 1998.

[106] Thomas JR Hughes. *The finite element method: linear static and dynamic finite element analysis*. Courier Corporation, 2012.

[107] David Pardo, Pawel J Matuszyk, Vladimir Puzyrev, Carlos Torres-Verdin, Myung Jin Nam, and Victor M Calo. *Modeling of Resistivity and Acoustic Borehole Logging Measurements Using Finite Element Methods*. Elsevier, 2021.

[108] Hong-lin Liao, Bingquan Ji, and Luming Zhang. An adaptive BDF2 implicit time-stepping method for the phase field crystal model. *IMA Journal of Numerical Analysis*, 42(1):649–679, 11 2020.

[109] E. Alberdi Celaya, J. J. Anza Aguirrezabala, and P. Chatzipantelidis. Implementation of an adaptive BDF2 formula and comparison with the MATLAB Ode15s. *Procedia Computer Science*, 29:1014–1026, 2014.

[110] P. Vignal, N. Collier, L. Dalcin, D.L. Brown, and V.M. Calo. An energy-stable time-integrator for phase-field models. *Computer Methods in Applied Mechanics and Engineering*, 316:1179–1214, 2017. Special Issue on Isogeometric Analysis: Progress and Challenges.

[111] Nicolás A. Labanda, Luis Espath, and Victor M. Calo. A spatio-temporal adaptive phase-field fracture method. *Computer Methods in Applied Mechanics and Engineering*, 392:114675, 2022.

[112] Ernst Hairer and Gerhard Wanner. *Solving Ordinary Differential Equations II: Stiff and Differential-Algebraic Problems*, volume 14. Springer, 2010.

[113] H. Gómez, V. M. Calo, Y. Bazilevs, and T. J.R. Hughes. Isogeometric analysis of the Cahn–Hilliard phase-field model. *Computer Methods in Applied Mechanics and Engineering*, 197(49):4333 – 4352, 2008.

[114] J. Lang. Two-dimensional fully adaptive solutions of reaction-diffusion equations. *Applied Numerical Mathematics*, 18(1):223 – 240, 1995.

[115] Martin S Alnæs, Jan Blechta, Johan Hake, August Johansson, Benjamin Kehlet, Anders Logg, Chris Richardson, Johannes Ring, Marie E Rognes, and Garth N Wells. The FEniCS project version 1.5. *Archive of Numerical Software*, 3(100):9–23, 2015.

[116] R. C. Kirby. Algorithm 839: FIAT, a new paradigm for computing finite element basis functions. *ACM Trans. Math. Softw.*, 30(4):502–516, 2004.

[117] Lisandro Dalcin and Yao-Lung L. Fang. mpi4py: Status update after 12 years of development. *Computing in Science Engineering*, 23(4):47–54, 2021.

[118] Lisandro D. Dalcin, Rodrigo R. Paz, Pablo A. Kler, and Alejandro Cosimo. Parallel distributed computing using Python. *Advances in Water Resources*, 34(9):1124–1139, 2011. New Computational Methods and Software Tools.

[119] Lisandro Dalcín, Rodrigo Paz, Mario Storti, and Jorge D'Elía. MPI for Python: Performance improvements and MPI-2 extensions. *Journal of Parallel and Distributed Computing*, 68(5):655–662, 2008.

[120] Lisandro Dalcín, Rodrigo Paz, and Mario Storti. MPI for Python. *Journal of Parallel and Distributed Computing*, 65(9):1108–1115, 2005.

[121] S. Balay, S. Abhyankar, M. Adams, J. Brown, P. Brune, K. Buschelman, L. Dalcin, A. Dener, V. Eijkhout, W. Gropp, D. Karpeyev, D. Kaushik, M. Knepley, D. May, L. Curfman McInnes, R. Mills, T. Munson, K. Rupp, P. Sanan, B. Smith, S. Zampini, H. Zhang, and H. Zhang. *PETSc Users Manual, ANL-95/11 - Revision 3.15*. 2021.

[122] Bradley Trembacki, Eric Duoss, Geoffrey Oxberry, Michael Stadermann, and Jayathi Murthy. Mesoscale electrochemical performance simulation of 3D interpenetrating lithium-ion battery electrodes. *Journal of The Electrochemical Society*, 166(6):A923–A934, 2019.

[123] Charles Monroe and John Newman. Dendrite growth in lithium/polymer systems. *Journal of The Electrochemical Society*, 150(10):A1377, 2003.

[124] L. Vitos, A.V. Ruban, H.L. Skriver, and J. Kollár. The surface energy of metals. *Surface Science*, 411(1):186–202, 1998.

[125] Richard Tran, Zihan Xu, Balachandran Radhakrishnan, Donald Winston, Wenhao Sun, Kristin A Persson, and Shyue Ping Ong. Surface energies of elemental crystals. *Scientific data*, 3(1):1–13, 2016.

[126] Lars Ole Valoen and Jan N. Reimers. Transport properties of $LiPF_6$-based Li-ion battery electrolytes. *Journal of The Electrochemical Society*, 152(5):A882, 2005.

[127] Kei Nishikawa, Hitoshi Naito, Makoto Kawase, and Tetsuo Nishida. Morphological variation of electrodeposited Li in ionic liquid. *ECS Transactions*, 41(41):3–10, dec 2019.

[128] Vladimir Yufit, Farid Tariq, David S. Eastwood, Moshiel Biton, Billy Wu, Peter D. Lee, and Nigel P. Brandon. Operando visualization and multi-scale tomography studies of dendrite formation and dissolution in zinc batteries. *Joule*, 3(2):485–502, 2019.

[129] Kei Nishikawa, Takeshi Mori, Tetsuo Nishida, Yasuhiro Fukunaka, Michel Rosso, and Takayuki Homma. In situ observation of dendrite growth of electrodeposited Li metal. *Journal of The Electrochemical Society*, 157(11):A1212, 2010.

[130] Hector Gomez and Thomas J.R. Hughes. Provably unconditionally stable, second-order time-accurate, mixed variational methods for phase-field models. *Journal of Computational Physics*, 230(13):5310–5327, 2011.

[131] A.F. Sarmiento, L.F.R. Espath, P. Vignal, L. Dalcin, M. Parsani, and V.M. Calo. An energy-stable generalized-α method for the Swift–Hohenberg equation. *Journal of Computational and Applied Mathematics*, 344:836–851, 2018.

[132] X. Wu, G. J. van Zwieten, and K. G. van der Zee. Stabilized second-order convex splitting schemes for Cahn–Hilliard models with application to diffuse-interface tumor-growth models. *International Journal for Numerical Methods in Biomedical Engineering*, 30(2):180–203, 2014.

[133] Andrea Hawkins-Daarud, Kristoffer G van der Zee, and J Tinsley Oden. Numerical simulation of a thermodynamically consistent four-species tumor growth model. *International journal for numerical methods in biomedical engineering*, 28(1):3–24, 2012.